UNIVERSITY OF AMSTERDAM

UvA-DARE (Digital Academic Repository)

X-Ray Polarization of the High-synchrotron-peak BL Lacertae Object 1ES 1959+650 during Intermediate and High X-Ray Flux States

Pacciani, Luigi; Vink, Jacco; Ng, C.Y.; IXPE

DOI
10.3847/1538-4357/adbbe2

Publication date
2025

Document Version
Final published version

Published in
Astrophysical Journal

License
CC BY

Link to publication

Citation for published version (APA):
Pacciani, L., Vink, J., Ng, C. Y., & IXPE (2025). X-Ray Polarization of the High-synchrotron-peak BL Lacertae Object 1ES 1959+650 during Intermediate and High X-Ray Flux States. *Astrophysical Journal*, *983*(1), Article 78. https://doi.org/10.3847/1538-4357/adbbe2

General rights
It is not permitted to download or to forward/distribute the text or part of it without the consent of the author(s) and/or copyright holder(s), other than for strictly personal, individual use, unless the work is under an open content license (like Creative Commons).

Disclaimer/Complaints regulations
If you believe that digital publication of certain material infringes any of your rights or (privacy) interests, please let the Library know, stating your reasons. In case of a legitimate complaint, the Library will make the material inaccessible and/or remove it from the website. Please Ask the Library: https://uba.uva.nl/en/contact, or a letter to: Library of the University of Amsterdam, Secretariat, P.O. Box 19185, 1000 GD Amsterdam, The Netherlands. You will be contacted as soon as possible.

UvA-DARE is a service provided by the library of the University of Amsterdam (https://dare.uva.nl)

Download date:08 Oct 2026

The Astrophysical Journal, 983:78 (20pp), 2025 April 10 https://doi.org/10.3847/1538-4357/adbbe2
© 2025. The Author(s). Published by the American Astronomical Society.
OPEN ACCESS

X-Ray Polarization of the High-synchrotron-peak BL Lacertae Object 1ES 1959+650 during Intermediate and High X-Ray Flux States

Luigi Pacciani[1], Dawoon E. Kim[1,2,3], Riccardo Middei[1], Herman L. Marshall[4], Alan P. Marscher[5], Ioannis Liodakis[6,7], Iván Agudo[8], Svetlana G. Jorstad[5,9], Juri Poutanen[10], Manel Errando[11], Laura Di Gesu[12], Michela Negro[13], Fabrizio Tavecchio[14], Kinwah Wu[15], Chien-Ting Chen[16], Fabio Muleri[1], Lucio Angelo Antonelli[17,18], Immacolata Donnarumma[12], Steven R. Ehlert[6], Francesco Massaro[19,20], Stephen L. O'Dell[6], Matteo Perri[17,18], Simonetta Puccetti[18], Francisco José Aceituno[8], Giacomo Bonnoli[8,14], Víctor Casanova[8], Juan Escudero[8], Beatriz Agís-González[8], César Husillos[8], Daniel Morcuende[8], Jorge Otero-Santos[8], Alfredo Sota[8], Pouya M. Kouch[10,21,22], Elina Lindfors[21], George A. Borman[23], José L. Gómez[8], Evgenia N. Kopatskaya[9], Elena G. Larionova[9], Daria A. Morozova[9], Sergey S. Savchenko[9,24,25], Andrey A. Vasilyev[9], Alexey V. Zhovtan[23], Dmitry Blinov[26,27,28], Anastasia Gourni[28], Sebastian Kiehlmann[7,28], Angelos Kourtidis[28], Nikos Mandarakas[7,28], Efthymios Palaiologou[7,28], Nikolaos Triantafyllou[28], Anna Vervelaki[28], Ioannis Myserlis[29,30], Mark Gurwell[31], Garrett Keating[31], Ramprasad Rao[31], Emmanouil Angelakis[32], Alexander Kraus[30], Matteo Bachetti[33], Luca Baldini[34,35], Wayne H. Baumgartner[6], Ronaldo Bellazzini[34], Stefano Bianchi[36], Stephen D. Bongiorno[6], Raffaella Bonino[19,20], Alessandro Brez[34], Niccoló Bucciantini[37,38,39], Fiamma Capitanio[1], Simone Castellano[34], Elisabetta Cavazzuti[12], Stefano Ciprini[18,40], Enrico Costa[1], Alessandra De Rosa[1], Ettore Del Monte[1], Niccoló Di Lalla[41], Alessandro Di Marco[1], Victor Doroshenko[42], Michal Dovčiak[43], Teruaki Enoto[44], Yuri Evangelista[1], Sergio Fabiani[1], Riccardo Ferrazzoli[1], Javier A. Garcia[45], Shuichi Gunji[46], Kiyoshi Hayashida[47], Jeremy Heyl[48], Wataru Iwakiri[49], Philip Kaaret[6], Vladimir Karas[43], Fabian Kislat[50], Takao Kitaguchi[44], Jeffery J. Kolodziejczak[6], Henric Krawczynski[11], Fabio La Monaca[1,2,3], Luca Latronico[19], Simone Maldera[19], Alberto Manfreda[51], Frédéric Marin[52], Andrea Marinucci[12], Giorgio Matt[36], Ikuyuki Mitsuishi[53], Tsunefumi Mizuno[54], C.-Y. Ng[55], Nicola Omodei[41], Chiara Oppedisano[19], Alessandro Papitto[17], George G. Pavlov[56], Abel Lawrence Peirson[41], Melissa Pesce-Rollins[34], Pierre-Olivier Petrucci[57], Maura Pilia[33], Andrea Possenti[33], Brian D. Ramsey[6], John Rankin[1], Ajay Ratheesh[1], Oliver J. Roberts[16], Roger W. Romani[41], Carmelo Sgró[34], Patrick Slane[31], Paolo Soffitta[1], Gloria Spandre[34], Douglas A. Swartz[16], Toru Tamagawa[44], Roberto Taverna[58], Yuzuru Tawara[53], Allyn F. Tennant[6], Nicholas E. Thomas[6], Francesco Tombesi[3,40,59], Alessio Trois[33], Sergey S. Tsygankov[10], Roberto Turolla[15,58], Jacco Vink[60], Martin C. Weisskopf[6], Fei Xie[1,61], and Silvia Zane[15]

[1] INAF, Istituto di Astrofisica e Planetologia Spaziali, Via Fosso del Cavaliere, 100 - I-00133 Rome, Italy; luigi.pacciani@inaf.it
[2] Dipartimento di Fisica, Università degli Studi di Roma "La Sapienza," Piazzale Aldo Moro 5, 00185 Roma, Italy
[3] Dipartimento di Fisica, Università degli Studi di Roma "Tor Vergata," Via della Ricerca Scientifica 1, 00133 Roma, Italy
[4] MIT Kavli Institute for Astrophysics and Space Research, Massachusetts Institute of Technology, 77 Massachusetts Avenue, Cambridge, MA 02139, USA
[5] Institute for Astrophysical Research, Boston University, 725 Commonwealth Avenue, Boston, MA 02215, USA
[6] NASA Marshall Space Flight Center, Huntsville, AL 35812, USA
[7] Institute of Astrophysics, Foundation for Research and Technology-Hellas, GR-71110 Heraklion, Greece
[8] Instituto de Astrofísica de Andalucía, IAA-CSIC, Glorieta de la Astronomía s/n, 18008 Granada, Spain
[9] Saint Petersburg State University, 7/9 Universitetskaya nab., St. Petersburg, 199034, Russia
[10] Department of Physics and Astronomy, University of Turku, 20014, Finland
[11] Physics Department and McDonnell Center for the Space Sciences, Washington University in St. Louis, St. Louis, MO 63130, USA
[12] ASI—Agenzia Spaziale Italiana, Via del Politecnico snc, 00133 Roma, Italy
[13] Department of Physics and Astronomy, Louisiana State University, Baton Rouge, LA 70803, USA
[14] INAF Osservatorio Astronomico di Brera, Via E. Bianchi 46, 23807 Merate (LC), Italy
[15] Mullard Space Science Laboratory, University College London, Holmbury St Mary, Dorking, Surrey RH5 6NT, UK
[16] Science and Technology Institute, Universities Space Research Association, Huntsville, AL 35805, USA
[17] INAF Osservatorio Astronomico di Roma, Via Frascati 33, 00078 Monte Porzio Catone (RM), Italy
[18] Space Science Data Center, Agenzia Spaziale Italiana, Via del Politecnico snc, 00133 Roma, Italy
[19] Istituto Nazionale di Fisica Nucleare, Sezione di Torino, Via Pietro Giuria 1, 10125 Torino, Italy
[20] Dipartimento di Fisica, Universitá degli Studi di Torino, Via Pietro Giuria 1, 10125 Torino, Italy
[21] Finnish Centre for Astronomy with ESO, University of Turku, 20014, Finland
[22] Aalto University Metsähovi Radio Observatory, Metsähovintie 114, FI-02540 Kylmälä, Finland
[23] Crimean Astrophysical Observatory RAS, P/O Nauchny, 298409, Crimea[62]
[24] Special Astrophysical Observatory, Russian Academy of Sciences, 369167, Nizhnii Arkhyz, Russia
[25] Pulkovo Observatory, St.Petersburg, 196140, Russia
[26] Foundation for Research and Technology—Hellas, IESL, Greece
[27] Institute of Astrophysics, Voutes, 7110, Heraklion, Greece
[28] Department of Physics, University of Crete, 70013, Heraklion, Greece
[29] Institut de Radioastronomie Millimétrique, Avenida Divina Pastora, 7, Local 20, E-18012 Granada, Spain
[30] Max-Planck-Institut für Radioastronomie, Auf dem Hügel 69, D-53121 Bonn, Germany
[31] Center for Astrophysics—Harvard & Smithsonian, 60 Garden Street, Cambridge, MA 02138, USA
[32] Section of Astrophysics, Astronomy & Mechanics, Department of Physics, National and Kapodistrian University of Athens, Panepistimiopolis Zografos 15784, Greece
[33] INAF Osservatorio Astronomico di Cagliari, Via della Scienza 5, 09047 Selargius (CA), Italy
[34] Istituto Nazionale di Fisica Nucleare, Sezione di Pisa, Largo B. Pontecorvo 3, 56127 Pisa, Italy
[35] Dipartimento di Fisica, Universitá di Pisa, Largo B. Pontecorvo 3, 56127 Pisa, Italy

[36] Dipartimento di Matematica e Fisica, Universitá degli Studi Roma Tre, Via della Vasca Navale 84, 00146 Roma, Italy
[37] INAF Osservatorio Astrofisico di Arcetri, Largo Enrico Fermi 5, 50125 Firenze, Italy
[38] Dipartimento di Fisica e Astronomia, Universitá degli Studi di Firenze, Via Sansone 1, 50019 Sesto Fiorentino (FI), Italy
[39] Istituto Nazionale di Fisica Nucleare, Sezione di Firenze, Via Sansone 1, 50019 Sesto Fiorentino (FI), Italy
[40] Istituto Nazionale di Fisica Nucleare, Sezione di Roma "Tor Vergata," Via della Ricerca Scientifica 1, 00133 Roma, Italy
[41] Department of Physics and Kavli Institute for Particle Astrophysics and Cosmology, Stanford University, Stanford, CA 94305, USA
[42] Institut für Astronomie und Astrophysik, Universität Tübingen, Sand 1, 72076 Tübingen, Germany
[43] Astronomical Institute of the Czech Academy of Sciences, Boční II 1401/1, 14100 Praha 4, Czech Republic
[44] RIKEN Cluster for Pioneering Research, 2-1 Hirosawa, Wako, Saitama 351-0198, Japan
[45] NASA Goddard Space Flight Center, Greenbelt, MD 20771, USA
[46] Yamagata University, 1-4-12 Kojirakawa-machi, Yamagata-shi 990-8560, Japan
[47] Osaka University, 1-1 Yamadaoka, Suita, Osaka 565-0871, Japan
[48] University of British Columbia, Vancouver, BC V6T 1Z4, Canada
[49] International Center for Hadron Astrophysics, Chiba University, Chiba 263-8522, Japan
[50] Department of Physics and Astronomy and Space Science Center, University of New Hampshire, Durham, NH 03824, USA
[51] Istituto Nazionale di Fisica Nucleare, Sezione di Napoli, Strada Comunale Cinthia, 80126 Napoli, Italy
[52] Université de Strasbourg, CNRS, Observatoire Astronomique de Strasbourg, UMR 7550, 67000 Strasbourg, France
[53] Graduate School of Science, Division of Particle and Astrophysical Science, Nagoya University, Furo-cho, Chikusa-ku, Nagoya, Aichi 464-8602, Japan
[54] Hiroshima Astrophysical Science Center, Hiroshima University, 1-3-1 Kagamiyama, Higashi-Hiroshima, Hiroshima 739-8526, Japan
[55] Department of Physics, The University of Hong Kong, Pokfulam, Hong Kong
[56] Department of Astronomy and Astrophysics, Pennsylvania State University, University Park, PA 16802, USA
[57] Université Grenoble Alpes, CNRS, IPAG, 38000 Grenoble, France
[58] Dipartimento di Fisica e Astronomia, Universitá degli Studi di Padova, Via Marzolo 8, 35131 Padova, Italy
[59] Department of Astronomy, University of Maryland, College Park, MD 20742, USA
[60] Anton Pannekoek Institute for Astronomy & GRAPPA, University of Amsterdam, Science Park 904, 1098 XH Amsterdam, The Netherlands
[61] Guangxi Key Laboratory for Relativistic Astrophysics, School of Physical Science and Technology, Guangxi University, Nanning 530004, People's Republic of China

Received 2024 October 30; revised 2025 February 19; accepted 2025 March 1; published 2025 April 8

Abstract

We report the Imaging X-ray Polarimetry Explorer (IXPE) polarimetric and simultaneous multiwavelength observations of the high-energy-peaked BL Lacertae object (HBL) 1ES 1959+650, performed in 2022 October and 2023 August. In 2022 October, IXPE measured an average polarization degree $\Pi_X = 9.4\% \pm 1.6\%$ and an electric-vector position angle $\psi_X = 53° \pm 5°$. The polarized X-ray emission can be decomposed into a constant component, plus a rotating component, with the rotation velocity $\omega_{EVPA} = (-117 \pm 12)$ deg day^{-1}. In 2023 August, during a period of pronounced activity of the source, IXPE measured an average $\Pi_X = 12.4\% \pm 0.7\%$ and $\psi_X = 20° \pm 2°$, with evidence (~0.4% chance probability) for a rapidly rotating component with $\omega_{EVPA} = 1864 \pm 34$ deg day^{-1}. These findings suggest the presence of a helical magnetic field in the jet of 1ES 1959+650 or stochastic processes governing the field in turbulent plasma. Our multiwavelength campaigns from radio to X-ray reveal variability in both polarization and flux from optical to X-rays. We interpret the results in terms of a relatively slowly varying component dominating the radio and optical emission, while rapidly variable polarized components dominate the X-ray and provide minor contribution at optical wavelengths. The radio and optical data indicate that on parsec scales the magnetic field is primarily orthogonal to the jet direction. On the contrary, X-ray measurements show a magnetic field almost aligned with the parsec jet direction. Confronting with other IXPE observations, we guess that the magnetic field of HBLs on subparsec scale should be rather unstable, often changing its direction with respect to the Very Long Baseline Array jet.

Unified Astronomy Thesaurus concepts: BL Lacertae objects (158); Polarimetry (1278); Relativistic jets (1390); High energy astrophysics (739); Plasma astrophysics (1261); Spectropolarimetry (1973); Blazars (164); Black holes (162); Active galaxies (17)

1. Introduction

Blazars are active galactic nuclei (AGN) with a relativistic jet of plasma pointing within several degrees of the line of sight (e.g., R. D. Blandford & A. Königl 1979). Relativistic motion (with bulk Lorentz factors $\Gamma \sim 10$) beams the radiation (C. M. Urry & P. Padovani 1995), causing these objects to be the most luminous persistent extragalactic sources at wavelengths from radio to TeV γ-ray. The nonthermal emission from the blazar jet can be extremely variable, on timescales as short as several minutes (F. Aharonian et al. 2007; M. Ackermann et al. 2016).

BL Lacertae objects are a class of blazars that exhibit little or no thermal emission, in lines or in continuum, in their near-IR, optical, and UV spectra. Hence, their spectral energy distribution (SED) is entirely dominated by nonthermal processes. High-energy-peaked BL Lac objects (HBLs) are a subclass with the SED of their synchrotron emission peaking at the X-ray energies.

The target of this investigation, 1ES 1959+650, is an HBL at redshift $z = 0.047$ (E. S. Perlman et al. 1996). It is among the first blazars detected at TeV energies (e.g., F. Aharonian et al. 2003), and it has been the target of several multifrequency campaigns (e.g., H. Krawczynski et al. 2004; G. Tagliaferri et al. 2008;

[62] While the AAS journals adhere to and respect UN resolutions regarding the designations of territories (available at http://www.un.org/press/en), it is our policy to use the affiliations provided by our authors on published articles.

Original content from this work may be used under the terms of the Creative Commons Attribution 4.0 licence. Any further distribution of this work must maintain attribution to the author(s) and the title of the work, journal citation and DOI.

E. Aliu et al. 2014; MAGIC Collaboration et al. 2020a). Very Long Baseline Array (VLBA) images obtained between 2005 and 2009 (and similarly for Mrk 501 and Mrk 421) at 22 GHz (B. G. Piner et al. 2010) revealed a characteristic polarization structure of the jet: the electric-vector position angle (EVPA) was parallel to the jet axis (position angle $\sim 150^{\circ}$, measured north through east) in the "core" (upstream end on the images) of the jet, while on the edges it was closer to orthogonal. This pattern can be interpreted in terms of a structured (spine-sheath) jet (B. G. Piner et al. 2010). Later, higher-resolution VLBA images at 43 GHz measured the jet direction in the most compact region to be $128^{\circ} \pm 13^{\circ}$ (Z. R. Weaver et al. 2022).

The EVPA of the optical polarization of 1ES 1959+650, observed between 2009 and 2011, varied about a stable value of $\sim 150^{\circ}$ (i.e., parallel to the compact jet; M. Sorcia et al. 2013). The authors speculated that two components are responsible for the optical emission, with one nearly stable component with EVPA $\sim 150^{\circ}$ associated with the overall jet emission, and a time varying component, perhaps originating in shocks within the jet.

The light curves of 1ES 1959+650 between 2016 and 2017 contain a number of flares from radio to TeV energies. These flux variations and the SED can be explained by a model with two electron populations: one with a synchrotron component peaking at radio-IR frequencies and another, highly variable component peaking in the X-ray range, with the optical emission corresponding to the superposition of both emitting components (S. R. Patel et al. 2018; MAGIC Collaboration et al. 2020a, 2020b); but see also B. Kapanadze et al. (2018) and S. Chandra et al. (2021) for different interpretations.

The Imaging X-ray Polarimetry Explorer (IXPE; M. C. Weisskopf et al. 2022) observed 1ES 1959+650 twice during the first semester of scientific operations. Polarization was detected during the first pointing (2022 May) with the polarization degree (PD) $\Pi_X = 8.0\% \pm 2.3\%$, although only an upper limit ($\Pi_X < 5.1\%$, 99% confidence level, c.l.) was obtained from the second observation (2022 June) of the source (M. Errando et al. 2024). During the second campaign, optical polarization at a level of $\Pi_O \sim 5\%$ was measured.

IXPE also observed the HBLs Mrk 421, and Mrk 501 during the first semester of scientific operations, detecting linear polarization in all of them (L. Di Gesu et al. 2022; I. Liodakis et al. 2022). The Mrk 501 observations found an almost constant X-ray PD and EVPA. In contrast with the second campaign of 1ES 1959+650, the X-ray PD was measured to be a factor of 2–2.5 times higher than at optical wavelengths, and the X-ray EVPA was found to be close to the optical and radio values, and also close to the direction of the jet axis. This is compatible with a model in which particles are accelerated at a shock front, after which they lose energy, leading to an energy-stratified emission region (I. Liodakis et al. 2022).

The first IXPE observation of Mrk 421 (L. Di Gesu et al. 2022) revealed a similar phenomenology as in the case of Mrk 501, but without alignment of the X-ray and optical EVPAs. Two subsequent IXPE observations of Mrk 421 found a rotation of the EVPA (L. Di Gesu et al. 2023). At the time of the X-ray EVPA rotation, the radio and optical PDs were lower than the X-ray values, and did not show any significant variation. During the second year of IXPE observations, four additional HBL objects were observed: 1ES 0229+200 (S. R. Ehlert et al. 2023), PG 1553+113 (R. Middei et al. 2023b), PKS 2155-304 (P. M. Kouch et al. 2024). These displayed behavior mostly consistent with that of Mrk 501. However, in the case of PG 1553+113, during the IXPE observation, an optical EVPA rotation was detected without a radio or X-ray counterpart.

Here, we report the results of two additional sets of IXPE and multiwavelength observations of 1ES 1959+650, one in 2022 late October and another in 2023 August. The latter campaign was triggered by an X-ray outburst (B. Kapanadze 2023).

Table 1
Log of X-Ray Observations

X-Ray Observatory	Observation Start (UT)	Exposure (ks)
IXPE	2022-10-28 06:02	281.6
XMM-Newton	2022-10-28 17:11	17.0
NuSTAR	2022-10-31 00:16	17.8
Swift-XRT	2022-10-29 09:39	0.9
…	2022-10-30 03:08	0.7
…	2022-10-31 01:16	1.7
IXPE	2023-08-14 01:09	459.7
Swift-XRT	2023-08-14 17:52	1.7
…	2023-08-15 19:12	1.7
…	2023-08-16 01:26	1.0
…	2023-08-16 23:58	0.8
…	2023-08-18 20:05	1.1
…	2023-08-19 00:52	0.8

2. Log of X-Ray Observations

The two sets of IXPE observations took place (1) between 2022 October 28 at 06:02 UT and 2022 October 31 at 12:16 UT (2022 October campaign); and (2) between 2023 August 14 at 01:09 UT and 2023 August 19 at 08:50 UT (2023 August campaign). During the 2022 October campaign, XMM-Newton observed the source starting on 2022 October 28 17:11 UT for 17.0 ks. MOS1 was operated in PrimePartialW2 mode with the thick filter, MOS2 in FastUncompressed mode with the medium filter, and p-n CCD in timing mode with the thick filter.

NuSTAR observed 1ES 1959+650 starting on 2022 October 31 at 00:16:09 UT for 17.8 ks, and Swift observed several times with the X-Ray Telescope (XRT), always operating in Windowed-Timing mode, and with the UVOT using all six filters.

During the 2023 August campaign, Swift observed the source with 1 day cadence with the XRT always in Windowed-Timing mode, and the UVOT using all six filters.

A summary of the X-ray observations is given in Table 1.

3. Data Analysis

3.1. IXPE Data

We used IXPE level 2 data, with photon-by-photon information on time of arrival, position, energy, and the Q and U Stokes parameters. We analyzed data using the publicly available IXPEOBSSIM software version 30.5.0 (L. Baldini et al. 2022). We extracted the source data from a circular region with a $1'.2$ radius centered on the source position, while we extracted background data from an annular region with $2'.5$ and $3'.5$ inner and outer radii, respectively. We used the `xpbin` procedure to obtain the polarization cube (PCUBE) and the Stokes parameter spectra (I, Q, and U); we subtracted the background by applying the procedure proposed in L. Baldini et al. (2022).

We generated source and background PCUBEs for each detector unit. Detector-by-detector spectra were produced for *I*, *Q*, *U* Stokes parameters using the PHAI, PHAQ, and PHAU methods in `xpbin` and applying calibration database version CALDB 20221020 and a background-to-source BACKSCALE ratio of 0.05. The weighted analysis algorithm proposed in A. Di Marco et al. (2022) was used with 075 response matrices for the spectral analysis. A light curve was produced starting with a bin size of 6 s. The time bins not contained in the good time intervals were rejected, while the others were grouped in order to obtain the final bin size.

3.2. Swift-XRT Data

We reduced Swift-XRT (D. N. Burrows et al. 2005) data using `xrtpipeline` version 0.13.4, included in the HEASOFT v6.25 package, and using the most recent available calibration files. Events with a grade 0–2 were selected for Window Timed (WT) data, and with a grade 0–12 for the photon counting mode. We used `xrtmkarf` to create the ancillary response files. Several Swift-XRT observations span more than a satellite orbit. In order to give a detailed light curve, we subdivided these observations on an orbit-by-orbit basis. The obtained source counting rate reported in the Swift-XRT light curve was then corrected for vignetting and for source signal lost in dead strips in WT mode.

3.3. NuSTAR Data

We made use of standard level 2 event files generated by the NuSTAR Science Operations Center and available from HEASARC archive. We reduced and analyzed NuSTAR data using the NUSTARDAS1 Data Analysis Software in the HEASOFT V6.29 package, adopting CALDB version 20211020 calibration files. We used the nuproducts tool to extract high-level science products for the source in the 3 −20 keV energy range. The source events were selected from a circular extraction region of 30″ radius, while the background was computed in an annulus centered on the source with inner and outer radii of 50″ and 100″ respectively.

3.4. XMM-Newton Data

We employed the XMM-Newton Science Analysis System, version 18.0.0, to process the XMM-Newton data. Source events were extracted from a circular region with 30″ radius centered on the source, while background events were obtained from a circular region with 40″ radius, offset from the source. Spectra were rebinned to have at least 30 counts for each spectral bin.

3.5. Swift/UVOT Data

We analyzed Swift-UVOT (P. W. A. Roming et al. 2005) data using the HEASOFT `uvotimsum` and `uvotsource` procedures. Source flux was extracted through aperture photometry from a 5″ circular region, and the UV magnitudes were corrected with values from Y. C. Pei (1992). Fluxes were derived from magnitudes according to T. S. Poole et al. (2008).

3.6. Radio/Optical Data

During the IXPE observations, several ground-based telescopes at radio (10−225 GHz) and optical (BVRI bands) frequencies provided total flux and polarization measurements. These included the Effelsberg 100 m telescope, the Submillimeter Array (SMA), Calar Alto Observatory, the LX-200 telescope operated by Saint Petersburg University, the Nordic Optical Telescope (NOT), the 1.8 m Perkins telescope owned by Boston University (Perkins Telescope Observatory), the T90 telescope at the Sierra Nevada Observatory (SNO), and the RoboPol 1.3 m telescope at Skinakas Observatory. Logs of optical and radio observations are given in Tables 2 and 3, respectively.

The Effelsberg 100 m telescope observations were taken at 10.45 and 17 GHz in 2023 July and August, as part of the QUIVER (monitoring the Stokes *Q*, *U*, *I*, and *V* emission of AGN jets in radio) monitoring program (A. Kraus et al. 2003; I. Myserlis et al. 2018). The SMA observations were obtained at 1.3 mm (225 GHz) on 2022 October 31, and several dates in 2023 August, within the SMA Monitoring of AGN with POLarization program. The observing setup involved orthogonally polarized receivers in full polarization mode. The polarized intensity, degree, and angle were derived from Stokes parameters *I*, *Q*, and *U* and calibrated using the MIR package[63] (R. J. Sault et al. 1995; D. P. Marrone & R. Rao 2008; R. A. Primiani et al. 2016).

The Calar Alto and Sierra Nevada observations were taken in *R* band using the CAFOS polarimeter and a set of polarized filters, respectively. Several observations were taken for several nights during each IXPE observation. For SNO, we used the weighted average of all the observations taken within the same night. The NOT observations were taken in the BVRI bands during both IXPE pointings, using the Alhambra Faint Object Spectrograph and Camera (ALFOSC). The observations and data reduction are described in detail in K. Nilsson et al. (2018). Additional photometric and polarimetric measurements in BVRI bands were obtained at the Perkins telescope (Flagstaff, AZ) from 2022 October 27 to 2022 November 1 using the PRISM camera. A general description of polarimetric observations can be found in S. G. Jorstad et al. (2010). The Skinakas observations were taken in *R* band during 2023 August using the four-channel RoboPol polarimeter mounted on the 1.3 m telescope (G. Panopoulou et al. 2015; D. Blinov et al. 2021). Finally, the LX-200 telescope provided *R*- and *I*-band total intensity and *R*-band polarimetric observations on 2022 October 30 and 2022 October 31, and BVRI photometry and *R*-band polarimetry during the 2023 August observation. A description of observational procedures and data reduction can be found in V. M. Larionov et al. (2008). More details on the IXPE-related multiwavelength observing strategy and data reduction can be found in I. Liodakis et al. (2022), R. Middei et al. (2023a), A. L. Peirson et al. (2023), P. M. Kouch et al. (2024), and L. Di Gesu et al. 2023). The *R*-band polarization measurements were corrected for dilution of the polarization by unpolarized host-galaxy starlight by subtracting its contribution within the apertures used by different observatories, following K. Nilsson et al. (2007) and T. Hovatta et al. (2016). For the remaining optical bands, we report the observed values.

4. Results

4.1. Light Curves and Hardness Ratios

The Swift-XRT and Swift-UVOT light curves are presented in Figure 1, covering the two observing campaigns. The first IXPE campaign was performed during a period of intermediate activity of the source, while the second was performed during a

[63] https://lweb.cfa.harvard.edu/~cqi/mircook.html

Table 2
Log of Optical Observations

Observatory	Filter	Date (UT)
NOT	B^p,V^p,R^pI^p	2022-10-30 20:09
⋯	B^p,V^p,R^pI^p	2022-10-31 20:52
Calar Alto	R^p	2022-10-29 20:25 (^{M})
⋯	R^p	2022-10-29 20:26 (^{M})
SNO	R	2022-10-27 22:38 (^{M})
⋯	R^p	2022-10-28 22:30 (^{M})
S. Petersburg	R^p,I	2022-10-30 16:24
⋯	R^p,I	2022-10-31 18:37
Perkins	R^p	2022-10-25 02:52 (^{M})
⋯	R^p	2022-10-26 02:52
⋯	V^p,I^p,B^p,R^p	2022-10-27 03:42
⋯	V^p,I^p,B^p,R^p	2022-10-28 03:12
⋯	V^p,I^p,B^p,R^p	2022-10-29 02:36
⋯	V^p,I^p,B^p,R^p	2022-10-29 04:22
⋯	V^p,I^p,B^p,R^p	2022-10-30 02:34
⋯	V^p,I^p,B^p,R^p	2022-10-30 04:25
⋯	V^p,I^p,B^p,R^p	2022-10-31 02:58
⋯	V^p,I^p,B^p,R^p	2022-10-31 04:52
⋯	V^p,I^p,B^p,R^p	2022-11-01 03:07
NOT	B^p,V^p,R^p,I^p	2023-08-14 02:52
⋯	B^p,V^p,R^p,I^p	2023-08-15 04:04
⋯	B^p,V^p,R^p,I^p	2023-08-17 03:07
⋯	B^p,V^p,R^p,I^p	2023-08-19 02:24
⋯	B^p,V^p,R^p,I^p	2023-08-20 07:12
⋯	B^p,V^p,R^p,I^p	2023-08-21 05:01
Calar Alto	R^p	2023-08-16 22:33 (^{M})
⋯	R^p	2023-08-18 02:09 (^{M})
SNO	R	2023-08-14 23:45
⋯	R	2023-08-18 00:43 (^{M})
⋯	R^P	2023-08-19 00:08 (^{M})
⋯	R^p	2023-08-20 00:28 (^{M})
⋯	R	2023-08-22 01:32
⋯	R	2023-08-24 22:04
⋯	R	2023-08-27 22:01
S. Petersburg	B,V,R^p,I	2023-08-14 22:19 (^{M})
⋯	B,V,R^p,I	2023-08-15 22:04 (^{M})
⋯	B,V,R^p,I	2023-08-17 21:43 (^{M})
⋯	B,V,R^p,I	2023-08-20 21:41 (^{M})
Skinakas	R^p	2023-08-03 19:26
⋯	R^p	2023-08-04 19:44
⋯	R^p	2023-08-05 19:59
⋯	R^p	2023-08-06 22:56
⋯	R^p	2023-08-16 18:16
⋯	R^p	2023-08-18 17:59
⋯	R^p	2023-08-20 17:47
⋯	R^p	2023-08-24 19:40
⋯	R^p	2023-08-26 22:17
⋯	R^p	2023-08-28 18:53

Note. The letter p on top of the filter flags a polarimetric measurement. The letter M after the observing date flags multiple observations during the same night. Swift-UVOT observations, performed with all six filters, were performed simultaneously to all the Swift-XRT observations reported in Table 1.

bright state. The IXPE light curves for the two periods are displayed in Figure 2.

The hardness ratio for the Swift-XRT data (defined as the ratio $(H-S)/(H+S)$ with H and S being the photon counts in the 2–10 keV and 0.3–2 keV bands, respectively) is shown in Figure 2; radio and optical light curves for the two campaigns are displayed in Figure 3.

Table 3
Log of Radio Observations

Observatory	Frequency (GHz)	Date (UT)
SMA	225	2022-11-10 07:07:24
SMA	225	2023-08-06 10:19
⋯	225	2023-08-16 06:57
⋯	225	2023-08-17 06:59
⋯	225	2023-08-18 07:55
⋯	225	2023-08-19 06:48
⋯	225	2023-08-20 07:26
Effelsberg	10.45, 17	2023-07-29 23:16
⋯	10.45, 17	2023-08-10 23:31
⋯	10.45, 17	2023-08-15 19:12
⋯	10.45, 17	2023-08-17 19:40
⋯	10.45, 17	2023-08-21 01:12

4.2. Polarimetry

4.2.1. X-Ray Polarimetry—2022 October Campaign

During the 2022 October observation, IXPE detected an average X-ray PD of $9.4\% \pm 1.6\%$ and an EVPA of $53^\circ \pm 5^\circ$, obtained by integrating over the entire 3.3 day pointing and over the energy interval 2−8 keV. For comparison, the minimum detectable polarization (corresponding to 99% c.l.) for that period was 4.9%.

The X-ray polarimetric evolution is shown in Figure 4 in q,u space, together with the constant polarization model. The result of fitting with a constant polarization model in q,u space is reported in the left panel of Figure 5 as a function of the number of time bins of the polarimetric light curve; the probability that the constant polarization model is correct is reported in the same figure. For the majority of chosen numbers of bins (except in four cases), the probability that the hypothesis of constant polarization is true is below 5%. Therefore, we evaluated other models to describe the polarimetric data.

We investigated the possibility of global EVPA rotation during the observation, e.g., the case where EVPA rotation applies to the entire time span of observed X-ray emission. We applied the unbinned likelihood method reported in L. Di Gesu et al. (2023), and we obtained an average global EVPA rotation rate $\omega_{\rm EVPA} = 5 \pm 4$ deg day^{-1} (error at the 68% c.l.); the rotation rate over the entire period is compatible with zero at 90% c.l.

The data reported in Figure 4, the IXPE observation of X-ray EVPA rotation in Mrk 421 (L. Di Gesu et al. 2023), and the claim of two components contributing to the optical polarization and to the broadband SED of 1ES 1959+650 motivated us to test two nested hypotheses: (a) The observed polarized X-rays have an EVPA that is steady, $\frac{d\psi}{dt} = 0$ (steady polarization case). (b) The emission has two superposed components: one with steady polarization and the other with variable EVPA with a constant rotation rate $\omega_{\rm EVPA}$ (two-component model). The two-component model differs from the global EVPA rotation model by adopting the hypothesis that the EVPA rotation is not a global phenomenon of the entire X-ray emission of the blazar; rather, it applies to only a fraction of the observed emission. The outcome of the tests of the two hypotheses is given in Table 4, where we report the results of the minimization of the unbinned log-likelihood estimators explained in Appendix A.

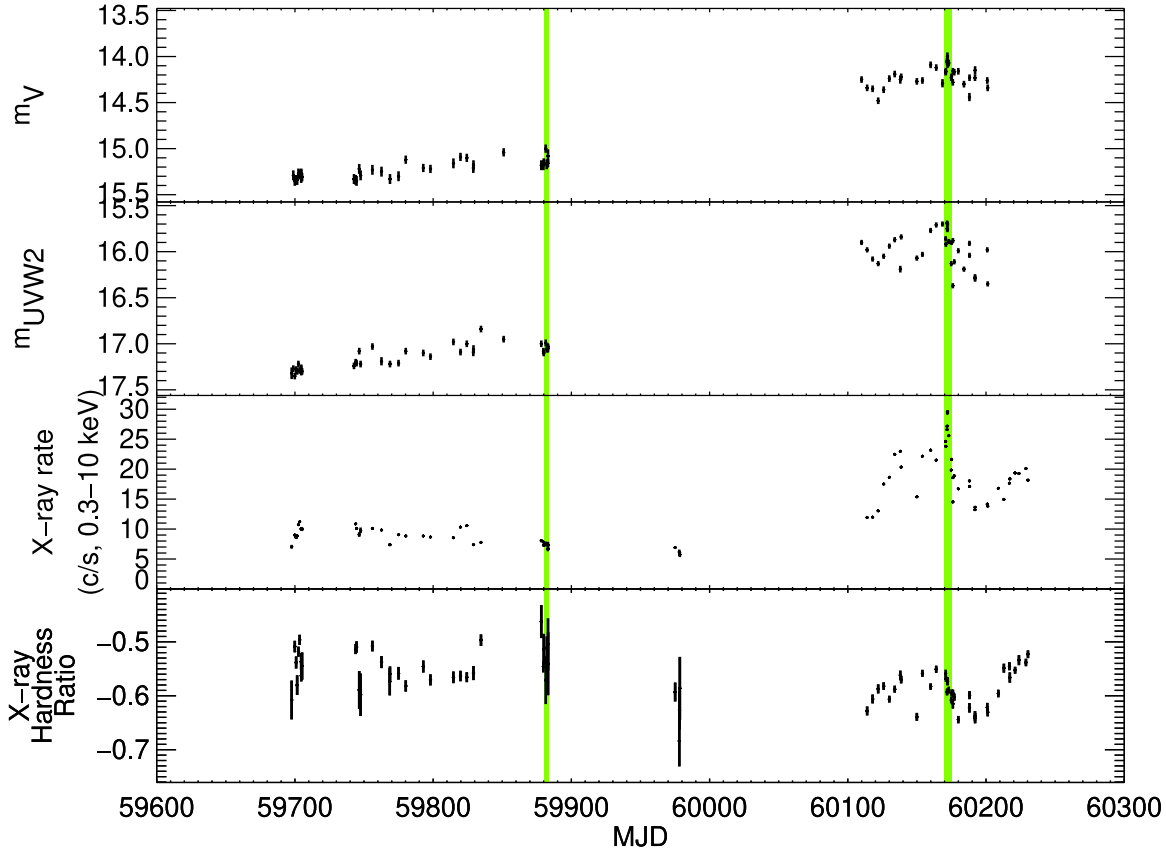

Figure 1. Swift light curves. Top to bottom: UVOT *V* optical filter, UVOT UVW2 ultraviolet filter, XRT X-ray, and X-ray hardness ratio (evaluated adopting the 0.3–2 keV and the 2–10 keV bands). The IXPE observing periods are denoted with green areas.

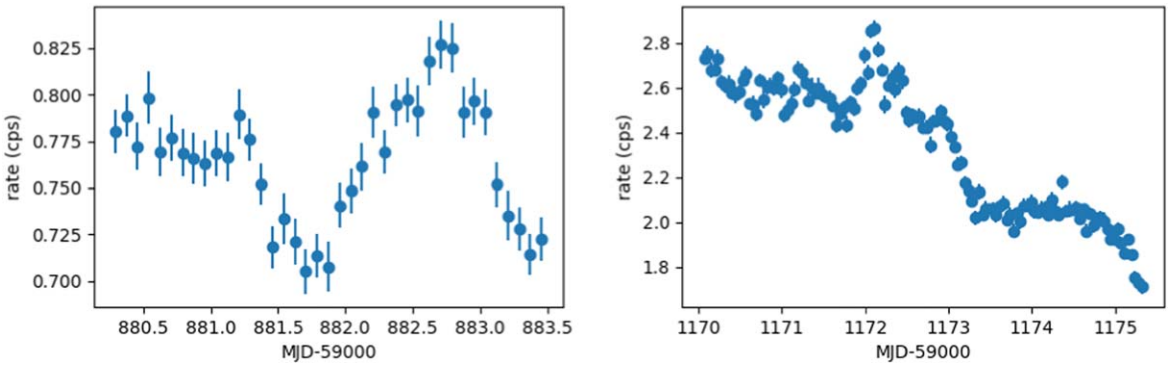

Figure 2. IXPE 2−8 keV light curves. Left: 2022 October campaign. Right: 2023 August campaign.

We derive a probability of 1.1×10^{-3} that the two-component model provides a better fit to the data (with respect to the constant polarization model) by random chance. The method for evaluating the statistical significance of the unbinned log-likelihood analysis is reported in Appendix C. We have checked the results of the unbinned log-likelihood study by adopting a binned analysis and χ^2 statistics. Details of this check are reported in Appendix C. The reduced χ^2 for the two-component model is 1.1 for 13 time bins.

The chosen two-component model assumes that the polarization variability is uncorrelated with the flux variability that we observe. We also tried a slightly different model, still consisting of a steady plus a variable component. We assumed that the component responsible for the polarization variability also causes flux variability, while the constant polarization component gives a steady contribution to the X-ray flux (flux-correlated two-component model). In this model, we added a parameter: the contribution of the constant component (component 1) to the count rate (r_1). By definition, r_1 cannot surpass the minimum source counting rate measured during the 2022 October observing period. In this model, there is no longer a degeneracy between R_1 and Π_1, or between R_2 and Π_2. Results of the fit are reported in Table 4. Note that the value of the r_1 parameter that minimizes the *C* estimator is at the upper bound of its allowed range (the minimum source counting rate during the observation).

The flux-correlated two-component model and the two-component model are not nested models, so we cannot compare these models directly. From the ΔC for the flux-correlated two-component model with respect to the steady

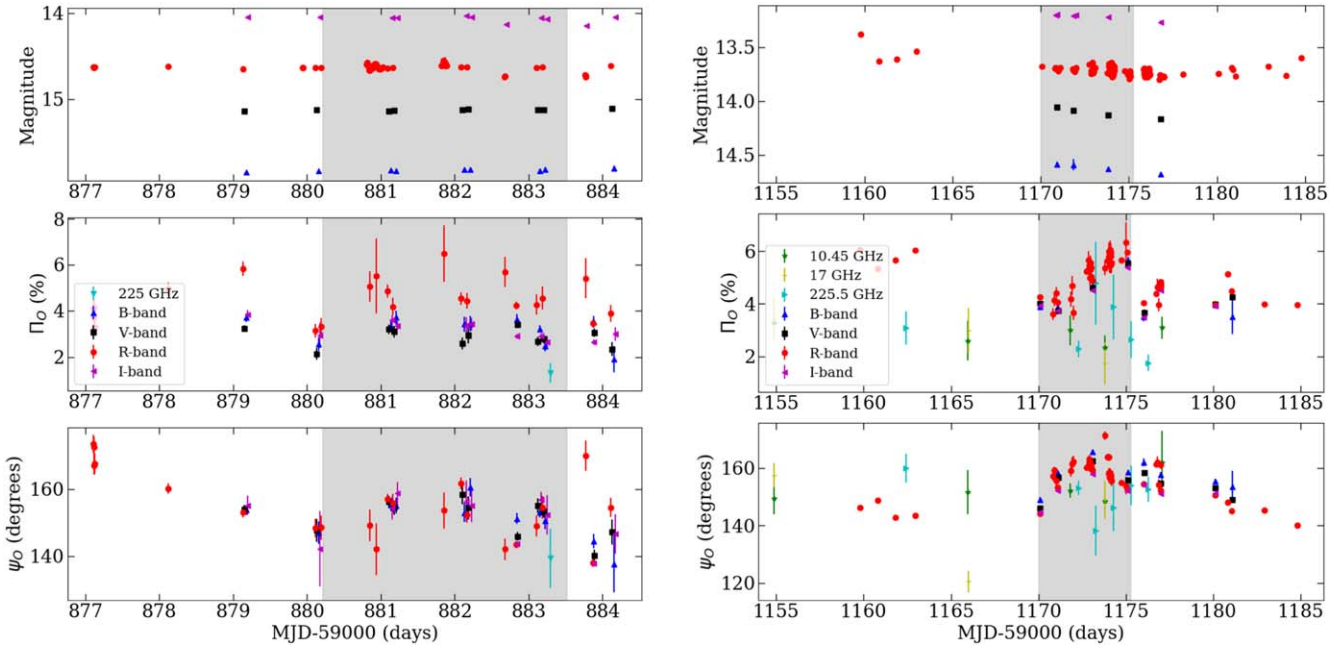

Figure 3. Radio and optical light curves and polarimetric measurements with ground-based telescopes. The 2022 October campaign in the left panel; the 2023 August campaign in the right panel. The panels from top to bottom show optical brightness, radio and optical PD, and radio and optical polarization angle. The duration of the IXPE observation is indicated by the gray shaded area.

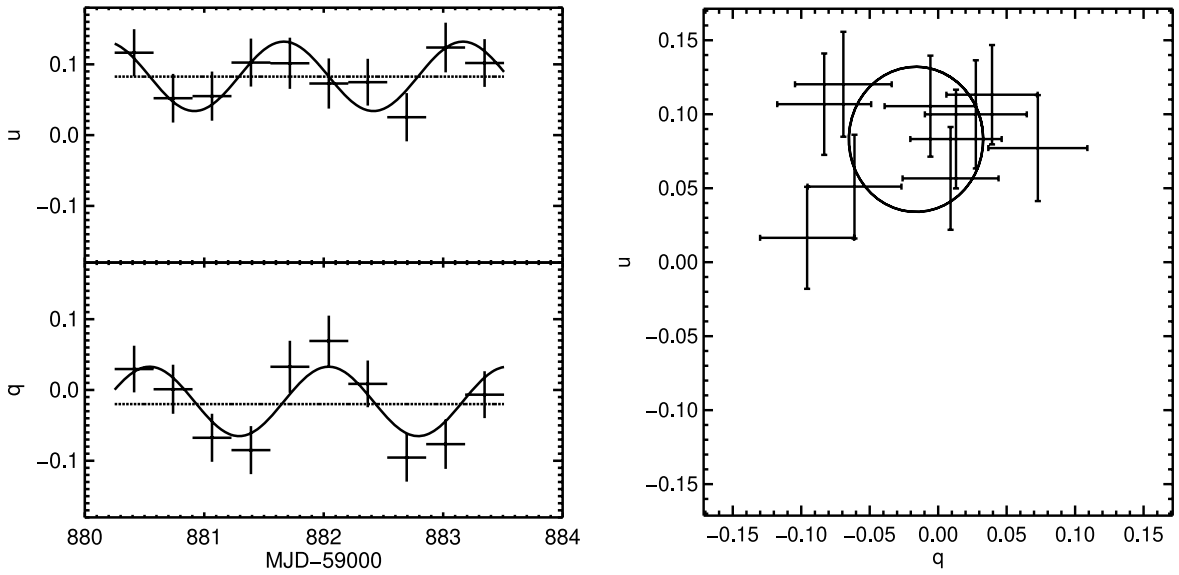

Figure 4. Left panel: Polarimetric evolution for the 2022 October observation. The constant polarization model (dotted line) and the two-component model (continuous line) are superposed on the data points. Right panel: q vs. u plot for the 2022 October observation. The continuous line is the two-component model fitting function.

polarization model, and from ΔC for the two-component model with respect to the steady polarization model, we obtain that the probability of choosing the flux-correlated two-component model by chance from a sample of events with steady polarization is about 1.8 times lower than the probability to choose the two-component model by chance.

4.2.2. X-Ray Polarimetry—2023 August Campaign

During the 2023 August pointing, IXPE detected an average PD of $12.4\% \pm 0.7\%$ and an EVPA of $19\overset{\circ}{.}7 \pm 1\overset{\circ}{.}7$. The measurements of q and u Stokes parameters as a function of time are reported in Figure 6. The fit with a constant polarization model is reported as well. The χ^2 binned analysis shows that the polarization cannot be considered constant with time.

We searched for a rotating component adopting the two-component model, with negative results. In fact, the two-component model produces a circular pattern in q, u space, while data show an elongated structure (Figure 6, central panel). Finally, we tried the three-component model (the new model has a constant component and two counterrotating components; see Appendix B). This model produces an ellipse in the q, u plane; therefore, it could reproduce the elongated pattern observed in 2023 August. The three component model has two more parameters with respect to the two-component model: the ratio $\frac{R_2^*}{R_2}\frac{\Pi_2^*}{\Pi_2}$ (where R_2^* is the relative flux of the

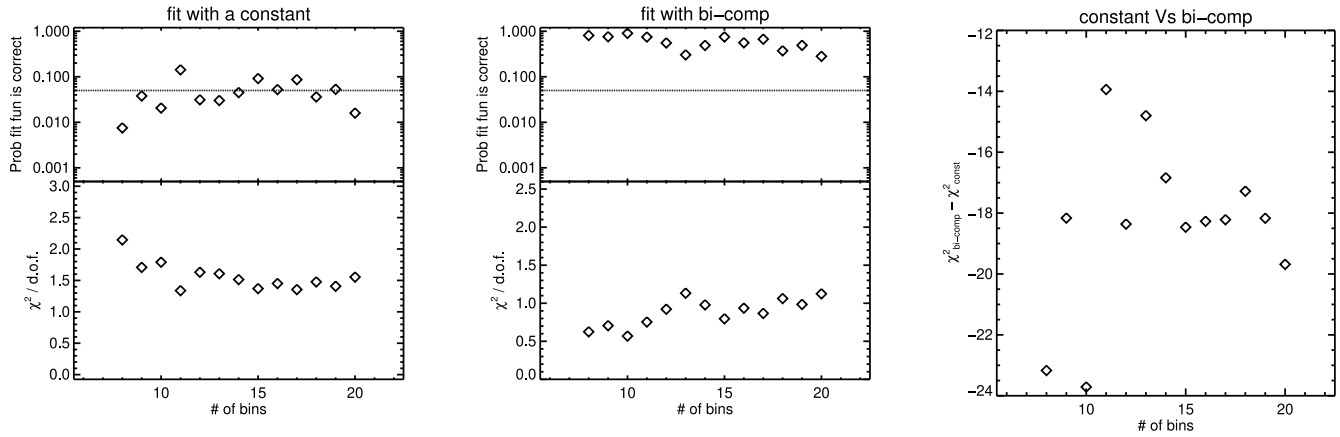

Figure 5. Results of binned analysis fitting of the 2022 October polarimetric light curve. Fit was performed on the q and u Stokes light curves. Left panel: reduced χ^2 for the constant polarization model as a function of the number of time bins, and associated probability that the fit function is true. Central panel: reduced χ^2 for the two-component polarization model as a function of the number of time bins, and associated probability that the fit function is true. Right panel: difference between the χ^2 for the two-component model and the χ^2 for the constant component as a function of the number of time bins (details are in Appendix C).

Table 4
Parameters and Log-likelihood Minima for the Steady Polarization Model, for the Two-component Model, and for the Flux-correlated Two-component Model for the 2022 October Observation of 1ES 1959+650 with IXPE

Steady Polarization Model		Two-component Model		Flux-correlated Two-component Model	
C	−62.2	C	−81.8	C	−85.3
Π(%)	9.4 ± 1.6	$R_1\Pi_1$(%)	$8.5^{+1.6}_{-1.9}$	Π_1(%)	10 ± 2
Ψ (deg)	53 ± 5	Ψ_1 (deg)	51 ± 6	Ψ_1 (deg)	50 ± 6
...	...	$R_2\Pi_2$(%)	4.9 ± 1.7	Π_2(%)	$62^{+0.21}_{-0.48}$
...	...	$\Psi_2(t=0)$ (deg)	31 ± 21	$\Psi_2(t=0)$ (deg)	25 ± 21
...	...	ω_2(deg day^{-1})	−117 ± 12	ω_2(deg day^{-1})	−117 ± 12
...	...	...	...	r_1 (cts s^{-1})	$0.71^{+0}_{-0.17}$

Note. C is the log-likelihood minimum, Π is the PD, and Ψ is the EVPA for the steady polarization model. The two-component model has five parameters: $R_1\Pi_1$ is the product of the relative flux with the PD of component 1, and $R_2\Pi_2$ is the same for component 2. Ψ_1 is the EVPA of component 1, $\Psi_2(t=0)$ is the EVPA of rotating component 2 at the beginning of the observation, and ω_2 is the angular velocity of the EVPA of the second component (see text). The flux-correlated two-component model has six parameters: Π_1 is the PD of component 1, and Π_2 is the same for component 2. Ψ_1 is the EVPA of component 1, $\Psi_2(t=0)$ is the EVPA of rotating component 2 at the beginning of the observation, ω_2 is the angular velocity of the EVPA of the second component, and r_1 is the count rate of the steady component.

counterrotating component, and Π_2^* is its PD), and the phase of the counterrotating component (see Appendix B for detail). In light of the pronounced flux variability during the observation, we have also searched for rotating components by dividing the sample into subintervals. We integrated data in windows whose lengths are half of the total observing time, and tried four time bins, shifting the bin by one-third of its size, to search for transient phenomena. Results for this staggered analysis are displayed in Figure 7.

We found a signal ($\Delta C = 26.6$ for 4 degrees of freedom, hereafter dof, plus the rotation-rate parameter, relative to the constant polarization model) at a rotation rate of 5.2 ± 0.1 turn day^{-1} (one turn is a 360° rotation of the EVPA) for an integration window of length $\Delta t = 2.66$ days, starting 1.77 days from the beginning of the observation. We report the results of this fit in Table 5.

We note that, when integrating data within the same window, there is another signal ($\Delta C = 20.5$) for a rotation rate of 1.9 ± 0.1 turn day^{-1}.

We have validated the unbinned log-likelihood analysis with a binned χ^2 test, as reported in Appendix D. The chance probabilities are $\leqslant 4.0 \times 10^{-3}$ and 6.5% for the candidate frequencies at 5.2 ± 0.1 and 1.9 ± 0.1 turn day^{-1}, respectively. We report the evaluation of the significance of the unbinned log-likelihood fit of the three-component model in Appendix D.

We report in Figure 8 (left panel) the X-ray PD and EVPA signals folded for a frequency of 5.2 ± 0.1 turn day^{-1}, accumulated for the entire window 3; and in Figure 8 (central panel) the corresponding q versus u plot.

The right panel of Figure 8 displays the folded polarimetric light curves in a 70° rotated q, u space. It shows that the modulated signal is almost unidimensional. We tested the hypothesis of an unidimensional oscillation by fixing the $\frac{R_2\,\Pi_2}{R_2\,\Pi_2 + R_2^*\,\Pi_2^*}$ parameter to 0.5. With this choice, the three-component model describes a line in q, u space, with Stokes parameters oscillating around the center of the line. With this choice, $\Delta C = -25.3$ for the principal minimum at 5.2 day^{-1} rotating frequency; while $\Delta C = -20.5$ for the secondary minimum at 1.9 day^{-1}. In this case, ΔC has a χ^2 distribution with 3 dof when computed as a function of the EVPA rotation rate. The probability to detect by chance at least two such signals with $\Delta C \leqslant -20.5$ in the 2023 August observation is $\leqslant 2.5 \times 10^{-4}$.

We have also investigated whether the rotation rate could vary with some power of X-ray energy: $\omega = \omega_0 \left(\frac{E}{2\ \mathrm{keV}}\right)^k$. For the 2022 October observation, we obtained $k = 0.1 \pm 0.1$; while for the 2023 August target of opportunity we obtained

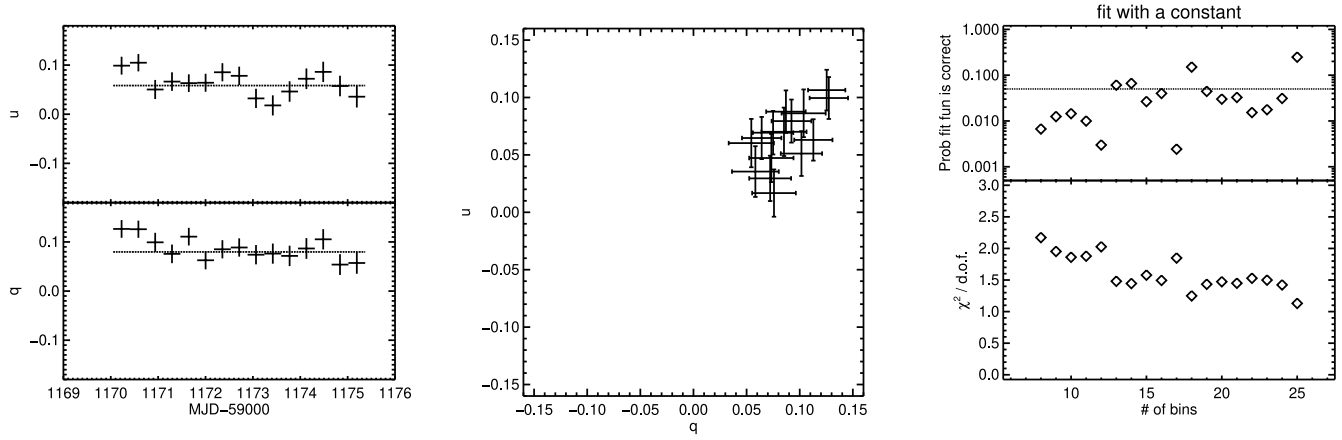

Figure 6. Polarimetric analysis of the 2023 August IXPE data. Fit was performed on the q and u Stokes light curves. Left panel: q and u light curves, fit with a constant polarization model. Central panel: q vs. u scatter plot for the 2023 August period. Right panel: reduced χ^2 for the constant polarization model as a function of the number of time bins, and associated probability that the fit function is true.

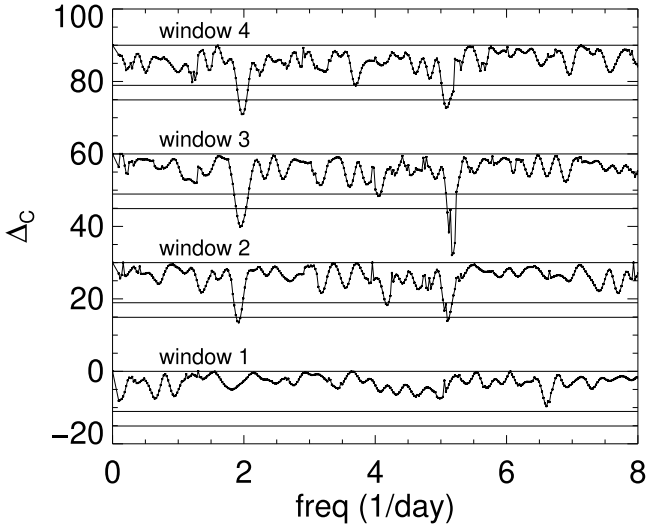

Figure 7. Result of search for rotating EVPA for the 2023 August data. We report the minimum of the log-likelihood estimator C for each candidate value of the rotation rate. Model consists of three components (with a rotating plus a counterrotating component). Results are shown for staggered windows of integration, with size 2.66 days, each shifted from the previous one by 0.88 day. For increasing window identifier, C is increased by multiples of 30.

$k = 0.002 \pm 0.005$ (90% c.l.). For both observations, the result is compatible with a rotation rate that does not vary with energy (90% c.l.). We have tested with simulations whether gaps in the observation or the satellite pointing dithering could produce a spurious rotating signal at the frequency range of our analysis, but were unable to reproduce such a signal. Details are given in Appendix D.

4.2.3. Radio and Optical Polarimetry

During the 2022 October campaign, we measured a low degree of polarization of 1ES 1959+650 at 225 GHz: $\Pi_R = 1.3\% \pm 0.4\%$ at a position angle of $\psi_R = 140^\circ \pm 9^\circ$. At optical wavelengths, the flux varied on short timescales, but with a low amplitude of <0.1 mag. The average intrinsic R-band polarization of the source was $\Pi_O = 4.54\% \pm 0.7\%$ at EVPA $\psi_O = 152^\circ \pm 6^\circ$. All B, V, R, and I EVPAs are consistent within uncertainties and appear to vary in tandem. The jet direction prior to 2018 was $128^\circ \pm 13^\circ$ (Z. R. Weaver et al. 2022), although during the IXPE observations it was (including uncertainties) ∼148°–168° (see below). Hence, the radio-optical polarization was roughly aligned with the jet axis within the rather large uncertainties.

Table 5
Parameters and Log-likelihood Minima for the Steady Polarization Model and for the Three-component Model with Two Counterrotating Components for the 2023 August Observation of 1ES 1959+650 with IXPE

Steady Polarization Model		Three-component Model with Two Counterrotating Components	
C	−187.4	C	−214.0
Π(%)	9.9 ± 1.2	$R_1\Pi_1$(%)	9.9 ± 1.2
Ψ (deg)	19 ± 2	Ψ_1 (deg)	19 ± 4
...	...	$R_2\Pi_2 + R_2^*\Pi_2^*$ (%)	5.3 ± 1.6
...	...	$\Psi_2(t=0)$ (deg)	65 ± 36
...	...	ω_2(deg day^{-1})	1864 ± 34
...	...	$\frac{R_2\Pi_2}{R_2\Pi_2 + R_2^*\Pi_2^*}$ (%)	55 ± 17
...	...	$\Psi_2^*(t=0)$ (deg)	3 ± 36

Note. C is the log-likelihood minimum, Π is the PD, and Ψ is the EVPA of the steady polarized component. The three-component model with two counterrotating components has seven parameters: $R_1\Pi_1$ is the product of the relative flux with the PD of component 1, Ψ_1 is the EVPA of component 1, $\Psi_2(t=0)$ and $\Psi_2^*(t=0)$ are the EVPAs of rotating and counterrotating components at the beginning of the observation, respectively, and ω_2 is the angular velocity of the EVPA of the rotating and counterrotating components. The other two parameters of the three-component model are $R_2\Pi_2 + R_2^*\Pi_2^*$ and $\frac{R_2\Pi_2}{R_2\Pi_2 + R_2^*\Pi_2^*}$, where R_2 and R_2^* are the relative fluxes of the rotating and counterrotating components, respectively, and Π_2 and Π_2^* are the PD of the rotating and counterrotating components (see Appendix B, Equation (B2)).

While the source was in an outburst during the 2023 August campaign, we did not observe significant differences in its radio-optical polarization properties. The flux exhibited similar fast variations at low amplitudes. The radio (10–225 GHz) polarization was in the range $\Pi_R = 1\%$–4% with EVPA between $\psi_R = 138^\circ$ and 159°, with a typical uncertainty $\sigma_{\psi_R} = 6^\circ$. The R-band polarization increased from 4% to 6% during the IXPE observation, and then returned to ∼4% afterward. The EVPA varied from 144° to 171°.

4.2.4. Millimeter-wave Imaging

The VLBA observes 1ES 1959+650 roughly monthly at a frequency of 43 GHz as part of the Blazars Entering the

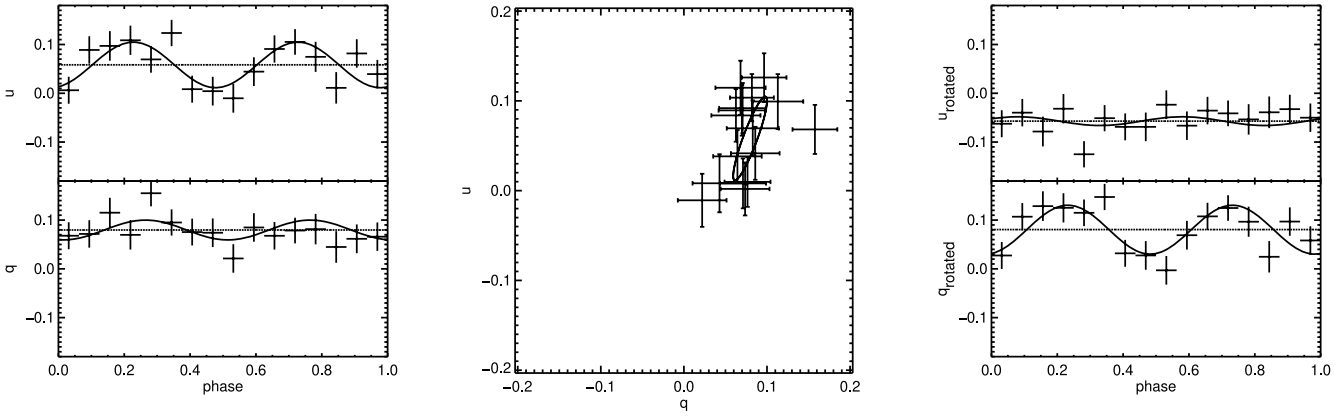

Figure 8. Left panel: Folded polarimetric light curve of X-ray q and u Stokes parameters, for a folding frequency of 5.2 ± 0.1 day^{-1}. Signal is accumulated for the entire window 3 of the 2023 August IXPE pointing (see text); the continuous line is the three-component model fitting function, while the dotted curve is the constant polarization model. Central panel: q vs. u plot for the folded signal; the ellipse (continuous line) is the three-component model fitting function. Right panel: folded polarimetric light curve of X-ray $q_{\rm rotated}$ and $u_{\rm rotated}$ Stokes parameters, rotated clockwise by 70° (the rotation angle corresponds to the angle of the ellipse (of the three-component model) major axis with respect to the q reference axis.)

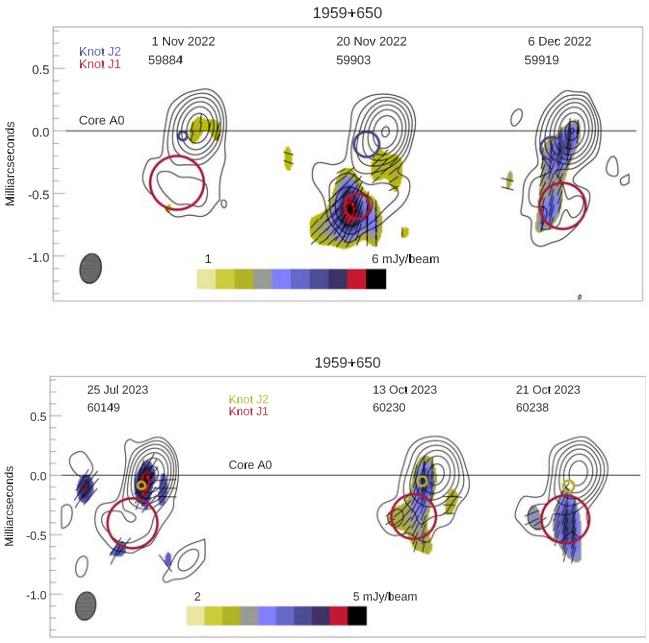

Figure 9. VLBA images at 43 GHz of 1ES 1959+650 at three epochs near each IXPE observation, which occurred in 2022 October 28–31 and 2023 August 14–19. Both calendar dates and MJDs of the images are given. Three emission features present in all images, A0 (the "core") J1, and J2, are marked, with their parameters listed in Table 6. Contours indicate total intensity in factors of 2, starting at 1.2% of the peak of 156 mJy beam^{-1} in 2022 and 255 mJy beam^{-1} in 2023. Color scale corresponds to linearly polarized intensity, with values indicated in each panel, while the polarization angle is denoted by the line segments in regions where polarization is detected. The elliptical restoring beam, with FWHM dimensions of 0.24×0.17 mas, with major axis along position angle $-10°$, is displayed in the lower left corner of each panel.

Astrophysical Multi-Messenger Era monitoring program.[64] In Figure 9, we present two sets of three images each, constructed from data obtained near each of the two IXPE epochs. The angular resolution is of the order 0.15 mas, which translates to 0.14 pc projected on the sky for a Hubble constant of 70 km s^{-1} Mpc^{-1}. The imaging process involves a number of calibration steps, followed by iterations of image construction and self-calibration; see S. G. Jorstad et al. (2017) for a thorough description of the analysis procedures. The object is weak at 43 GHz, limiting the dynamic range of the images such that the lowest contours are affected by noise. In order to represent the main features of each image, we fit the u–v data with three components of circular Gaussian brightness distributions. Table 6 lists the parameters of these components at each epoch. The brightest feature, A0, is referred to as the "core." In blazars, the core is considered stationary and near the upstream end of the jet. Knots (J1 and J2 in 1ES 1959+650) downstream of the core can either be quasi-stationary (common in BL Lac objects) or move away from the core (S. G. Jorstad et al. 2017). The only motion apparent in the images of Figure 9 is a downstream shift in the position of knot J1 between 2022 November 1 and 20 that does not continue to the next epoch 16 days later.

The jet direction (defined by a line between the centers of the core and knot J1) is $163° \pm 5°$ during the 2022 epochs and $155° \pm 2°$ in 2023. This is similar to the optical polarization angle. The degree of polarization of knot J1 tends to be high—up to $36\% \pm 16\%$—although the uncertainties are large. The 43 GHz polarization angles of the core and knots, when detected, are within $\pm 10°$ of the jet direction as well.

4.3. Energy Spectra

4.3.1. 2022 October Campaign

The X-ray spectrum obtained during the 2022 October campaign is shown in Figure 10. Data from Swift-XRT, IXPE, XMM-Newton, and NuSTAR are reported. An absorbed log-parabola model was fit to the data. Fit parameters are reported in Table 7. We obtained an unabsorbed flux of $(8.61 \pm 0.04) \times 10^{-11}$ erg cm^{-2} s^{-1} in the 2−8 keV band (90% c.l.).

4.3.2. 2023 August Campaign

Swift observed the blazar six times during the 2023 August IXPE observation. We derived the spectrum by integrating IXPE data over 1.0 day around the peak emission on MJD 60172. The spectrum thus obtained is displayed in Figure 10, while the fit parameters are reported in Table 8. We obtained an unabsorbed flux of $(31.4 \pm 0.6) \times 10^{-11}$ erg cm^{-2} s^{-1} (90% c.l.) in the 2–8 keV band.

[64] www.bu.edu/blazars/BEAM-ME.html

Table 6
Parameters of Knots in 43 GHz VLBA Images

Date	MJD	ID	Flux Density (mJy)	Distance from A0 (mas)	Position Angle (deg)	Diameter (mas)	Π (%)	χ (deg)
(1)	(2)	(3)	(4)	(5)	(6)	(7)	(8)	(9)
2022/11/01	59884	A0	117 ± 15	0.000	⋯	0.043 ± 0.005	1.5 ± 1.1	169 ± 11
		J2	6 ± 3	0.14 ± 0.01	99 ± 9	0.068 ± 0.007	<1.6	⋯
		J1	37 ± 9	0.42 ± 0.04	168 ± 6	0.43 ± 0.04	<16	⋯
2022/11/20	59903	A0	125 ± 17	0.000	⋯	0.040 ± 0.005	<0.6	⋯
		J2	35 ± 7	0.15 ± 0.01	136 ± 8	0.20 ± 0.01	<1.9	⋯
		J1	33 ± 9	0.68 ± 0.05	156 ± 6	0.20 ± 0.02	36 ± 16	151 ± 10
2022/12/06	59919	A0	149 ± 10	0.000	⋯	0.030 ± 0.004	2.2 ± 1.5	173 ± 5
		J2	24 ± 6	0.15 ± 0.01	126 ± 8	0.18 ± 0.01	7.1 ± 4.8	169 ± 11
		J1	26 ± 9	0.60 ± 0.04	165 ± 6	0.37 ± 0.02	43 ± 24	167 ± 16
2023/07/25	60149	A0	232 ± 12	0.000	⋯	0.022 ± 0.004	1.5 ± 0.8	138 ± 10
		J2	38 ± 9	0.110 ± 0.013	141 ± 10	0.063 ± 0.006	3.6 ± 1.5	155 ± 8
		J1	73 ± 11	0.40 ± 0.04	151 ± 9	0.42 ± 0.06	<21	⋯
2023/10/13	60230	A0	111 ± 10	0.000	⋯	0.039 ± 0.005	<1.1	⋯
		J2	70 ± 8	0.14 ± 0.01	152 ± 11	0.081 ± 0.007	7.1 ± 4.6	169 ± 10
		J1	42 ± 12	0.40 ± 0.01	149 ± 9	0.38 ± 0.04	23 ± 17	145 ± 21
2023/10/21	60238	A0	122 ± 15	0.000	⋯	0.025 ± 0.006	<0.8	⋯
		J2	62 ± 9	0.15 ± 0.02	160 ± 11	0.09 ± 0.01	<6.5	⋯
		J1	43 ± 11	0.44 ± 0.04	148 ± 8	0.40 ± 0.05	29 ± 21	155 ± 21

5. Discussion

Our X-ray observations found 1ES 1959+650 to be at an intermediate flux level in 2022 October and in an outburst in 2023 August. During the second campaign, the X-ray spectrum gradually softened as the flux declined, except for a brief period of hardening corresponding to the flux peak on MJD 60172. This can be interpreted as gradual cooling of the electron population, interrupted by an episode of enhanced acceleration of electrons.

Optical photometry in 2023 August measured the brightness to be 1.2−1.5 mag higher than in 2022 October. In contrast, the millimeter-wave flux did not vary significantly between the two epochs. The Swift-UVOT flux in 2023 August did not exhibit the flaring episode that peaked on MJD 60172, as observed in the X-ray range with both IXPE and Swift-XRT. Swift-UVOT observations with optical filters only showed a weak flux peak on MJD 60172.

For both periods, the optical PD was in the 4%−6% range, and the EVPA fluctuated within 15° of 153°. IXPE observations in 2022 October and 2023 August measured the PD and EVPA to change from 9.4% ± 1.6% to 12.4% ± 0.7%, and from 53° ± 5° to 12.°4 ± 0.7°, respectively.

Interestingly, the *R*-band PD in 2023 August increased from ∼4% to ∼6% from the beginning to the end of the IXPE pointing, while the EVPA varied more erratically by ±10°. In contrast, IXPE found higher X-ray polarization, without any increasing PD trend; see Figure 6.

Our IXPE measurements have found significant X-ray polarization, with evidence for a component with rotating EVPA during both observations. We have found that the EVPA rotation rate does not vary with X-ray energy. Electrons incoherently gyrating in a magnetic field follow the field lines, with EVPA orthogonal to the local magnetic field direction as projected on the sky. Plasma moving in a helical magnetic field will produce synchrotron radiation with a rotating EVPA when observed close to the symmetry axis of the helix.

We have found some evidence for a rapidly rotating (∼5.2 turn day^{-1}, 0.22% chance probability) component starting 1.77 days from the beginning of the 2023 August observation, which suggests that the rotation began with the peak in activity of the source. We found this signal only by adding a counterrotating component to the two-component model. In general, a rotating plus a counterrotating component describe an ellipse in the (q, u) plane (see Appendix B). In our case, the two components had almost the same flux, so that the model location in the (q, u) plane lies along a nearly straight line. Our three-component model reproduces the X-ray polarimetric variability observed for window 3 of the 2023 August IXPE pointing. However, we cannot establish if there was a counterrotating component responsible for the observed emission, or if, on the contrary, the counterrotating component only allowed us to describe a one-dimensional oscillation in the (q, u) plane caused by a different emission mechanism. A further rotating signal (∼1.9 turn day^{-1}) with lower significance is found for the same exposure time during the 2023 August campaign.

Two previous papers (L. Di Gesu et al. 2023; D. E. Kim et al. 2024) have discussed how helical motion of plasma could explain the phenomenology observed in Mrk 421. For a helix, we can define the instantaneous rising angle ($\Theta_{\rm rise}$) of the plasma moving along the helical path (see Figure 11), while the angle formed by the instantaneous velocity vector of plasma moving along a helical path and the symmetry axis of the helix is denoted by $\Theta_{\rm rise}^{\rm compl}$. (By definition, $\Theta_{\rm rise}^{\rm compl} = \frac{\pi}{2} - \Theta_{\rm rise}$.) We note that, for the rotating signal to be detected along the entire helical orbit, $\Theta_{\rm rise}^{\rm compl}$ should be smaller than the critical jet viewing angle $1/\Gamma_{\rm bulk}$. Moreover, the observer's viewing angle ($\Theta_{\rm view}$, measured with respect to the axis of the helix) should be lower than $\Theta_{\rm rise}^{\rm compl}$ for the Stokes parameters to execute a circular shape in the q, u plane:

$$\begin{cases} \Theta_{\rm rise}^{\rm compl} < 1/\Gamma_{\rm bulk} \\ \Theta_{\rm view} < \Theta_{\rm rise}^{\rm compl}. \end{cases} \quad (1)$$

This implies that the plasma's helical path is elongated along the jet axis.

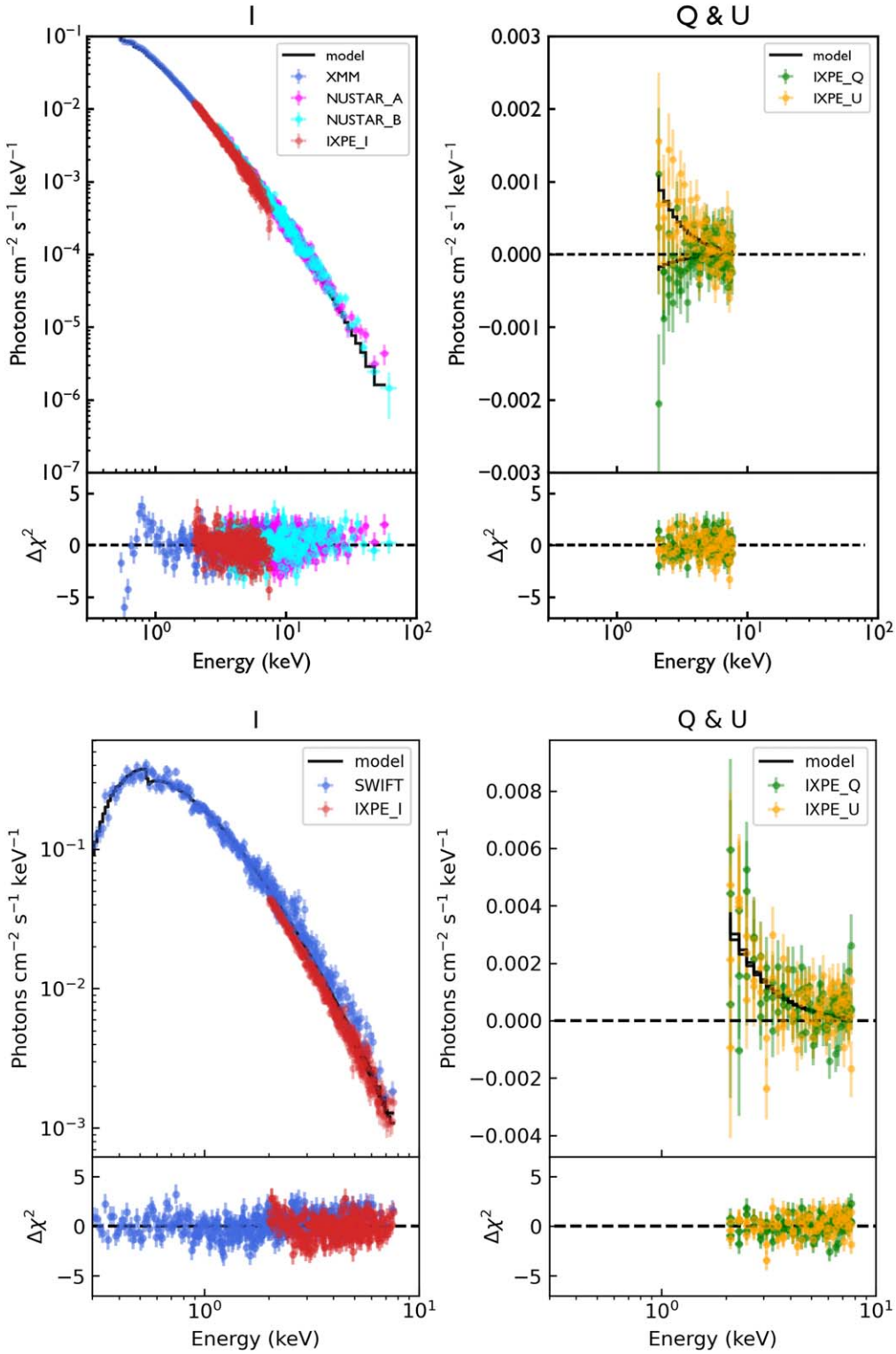

Figure 10. Top: combined X-ray spectrum of 1ES 1959+560 during the 2022 October multiwavelength campaign, including Swift-XRT, IXPE, XMM-Newton, and NuSTAR data. Bottom: combined X-ray spectrum during the 2023 August campaign, including Swift-XRT and IXPE data integrated for 1.0 day around the peak emission on MJD 60172.

The EVPA rotation observed in the 2022 October X-ray data of 1ES 1959+650 can be explained by the hypothesis corresponding to Equation (1). We note, however, that the observed X-ray polarization evolution can be interpreted also with the flux-correlated two-component model. With this modeling, we obtained that the fitted flux of the constant component corresponds to the maximum allowed value (see Table 4), possibly indicating that the line of sight was not inside the source emitting cone for the entire observation, $\Theta_{\rm view} \sim \Theta_{\rm rise}^{\rm compl}$, or, alternatively, that the typical opening angle of the helix is comparable to (or slightly larger than) the emitting cone aperture: $\Theta_{\rm rise}^{\rm compl} \sim 1/\Gamma_{\rm bulk}$.

Table 7
Log-parabola Model X-Ray Spectral Fit of the Combined 2022 October IXPE, NuSTAR, XMM-Newton, and Swift-XRT Data of 1ES 1959+650

$\frac{\chi^2}{\mathrm{dof}}$	dof	N_{H} (10^{21} cm^{-2})	Π_{X} (%)	Ψ_{X} (deg)	α	β	E_{pivot} (keV)	N (10^{-3} keV^{-1}cm^{-2})
1.22	1214	1.01	9.8 ± 1.2	50 ± 4	2.504 ± 0.005	0.323 ± 0.005	5	1.403 ± 0.005

Note. The number of degrees of freedom are denoted with dof; the column density N_{H} and pivot energy are held constant. Not shown in the table are the intercalibration factors with respect to XMM-Newton; for NUSTAR PFMA and PFMB, 1.14 ± 0.01 and 1.14 ± 0.01, respectively; for IXPE DU1, DU2, DU3, 1.033 ± 0.005, 0.991 ± 0.005, and 0.936 ± 0.005, respectively.

Table 8
X-Ray Spectral Fit of a Log-parabola Model to the Combined 2023 August IXPE and Swift-XRT Data for 1ES 1959+650

$\frac{\chi^2}{\mathrm{dof}}$	dof	N_{H} (10^{21} cm^{-2})	Π_{X} (%)	Ψ_{X} (deg)	α	β	E_{pivot} (keV)	N (10^{-3} keV^{-1}cm^{-2})
1.12	787	1.01	12.6 ± 1.3	22 ± 3	2.98 ± 0.02	0.80 ± 0.02	5	4.65 ± 0.06

Note. The number of degrees of freedom is denoted with dof; the column density N_{H} and pivot energy are held constant. The intercalibration factors, not shown in the table, are with Swift-XRT as reference: IXPE DU1, DU2, DU3, 0.873 ± 0.009, 0.829 ± 0.009, 0.793 ± 0.009, respectively.

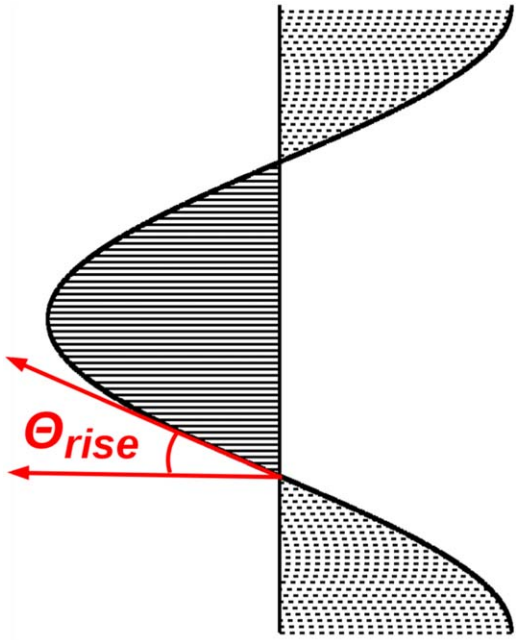

Figure 11. Helix viewed at 90° to the axis, illustrating the definition of the rising angle Θ_{rise}, the regions seen from above (shading by continuous lines), and regions seen from below (dashed lines). The jet axis corresponds to the vertical line.

The peculiar rotation of the EVPA observed in 2023 August cannot be explained with Equation (1). We also could not reproduce the observed behavior with the hypothesis that the our line of sight is outside $\Theta_{\mathrm{rise}}^{\mathrm{compl}}$:

$$\begin{cases} \Theta_{\mathrm{rise}}^{\mathrm{compl}} < 1/\Gamma_{\mathrm{bulk}} \\ \Theta_{\mathrm{view}} > \Theta_{\mathrm{rise}}^{\mathrm{compl}}. \end{cases} \quad (2)$$

The evolution of rotated Stokes parameters in Figure 8 suggests that the polarimetric oscillation takes place in a single dimension. Alternatively, we have the unlikely case of two almost exactly counterrotating (and of similar flux) components combining to give rise to the observed polarimetric X-ray signal.

EVPA rotation components could be a sign of a stochastic process controlling the direction of the magnetic field. Rotations that vary the EVPA about a "preferred" value can be explained also by turbulent plasma whose field is partially ordered by a shock or by a helical component (A. P. Marscher 2014).

6. Interpretation

The two campaigns centered on IXPE observations of 1ES 1959+650 found different X-ray PDs and EVPAs, which indicates that the X-ray polarization is not simply associated with a fixed jet direction. We propose that the polarized X-ray emission was associated with localized regions during each of the two campaigns, although there were substantial differences. During both observations, we detected evidence for components with rotating EVPAs. Over the intermediate activity period observed during the 2022 October campaign, the EVPA rotation velocity was low (∼0.3 turn day^{-1}). Our modeling of the IXPE data from the 2023 August campaign, during a major outburst of the source, instead found a fast rotation velocity (∼5.2 turn day^{-1}, detected when integrating data over 2.66 days). Another difference between the two campaigns is that, in 2022 October, we only needed a constant and a single rotating component, while, in the 2023 August campaign, a counterrotating component with almost the same intensity as the rotating one is required for the rotating EVPA signal to be detected, resulting in an elongated elliptical path in q, u space. There may be an analogy with solar coronal loop observations (see, e.g., V. M. Nakariakov et al. 2016, and references therein): both rapidly decaying and undamped oscillations are detected. For coronal loops, continuous excitation of the oscillating system is invoked to explain the latter case.

Regarding optical polarization, our data confirm the presence of a dominant and persistent polarized emission component with a fixed EVPA direction, with other weak components contributing to minor changes of the EVPA. We observed for the X-ray outburst in 2023 August a gradual rise of the optical PD, and a coincident change of the optical EVPA. Moreover, optical and UV photometric measurements show that, over long time spans, the optical and X-ray emission both rose in 2023 August with respect to emission in 2022 October, and that the X-ray flux peak on MJD 60172 was observed in V band as

well. Therefore, a dominant and persistent optical emission component is observed, but the data suggest that the plasma responsible for the X-ray emission provides a minor contribution to the optical flux.

In contrast with the X-ray emission, the optical polarization vector in 2023 August was, on average, oriented in a direction similar to that measured in 2022 October, even though the optical flux on 2023 August was double the level of 2022 October. This discrepancy can be reconciled by assuming that the X-rays are emitted within small regions where the mean direction of the magnetic field is not perpendicular to the jet axis as measured at 43 GHz, while optical photons are emitted from larger regions where the average magnetic field is transverse to the jet axis; see below for proposed models.

Regarding the radio flux and polarization, our data set is rather sparse for the 2022 October period, while for the 2023 August campaign the cadence is daily. The average radio PD is lower than the optical value, while the EVPA almost matches that at optical wavelengths. This suggests that the main source of radio flux has the same general origin as the dominant and persistent emission observed at optical wavelengths.

B. G. Piner et al. (2010) measured the apparent speed of moving components near the core at 43 GHz in TeV-detected blazars, finding low apparent speeds (below $1c$) for 1ES 1959 +650, Mrk 421, and Mrk 501, implying a viewing angle $\Theta_{view} < \frac{1}{\Gamma_{bulk}^2 \beta}$, and $\Gamma_{\rm bulk} \sim 3-5$. We argue for a similar scenario for the X-ray emission (see Equation (1)). At such a narrow viewing angle, the resolution of the VLBA images, $\sim$0.2 mas, corresponds to parsec scales when deprojected.

Z. R. Weaver et al. (2022) display an image of the blazar obtained in 2018 July at 43 GHz, showing the core A0, and knots A1, A2, A3, A4. A line of sight very close to the jet direction explains the rather large apparent opening angle, as well as the bend to the north on kiloparsec scales (T. A. Rector et al. 2003), which can be a small bend amplified by projection effects if the viewing angle is near 0°. (The jet direction is obtained from the position angle of lines connecting the core to the other features; position angles vary from $124° \pm 8°$ to $163° \pm 17°$; Z. R. Weaver et al. 2022.) Our similar high-resolution 43 GHz VLBA images in 2022 and 2023 (Figure 9) contain two features, J1 and J2, southeast of the core, with the inner jet EVPA oriented in the jet direction, indicative of a mean magnetic field that is transverse to the jet on parsec scales.

Polarization measurements at 10.45, 17, 43, and 225 GHz are core dominated, and they represent the average jet polarization on parsec scales (the innermost jet region is obscured by self-absorption at the lower frequencies), with EVPA aligned with the jet direction. We surmise that the observed PD is low because of a dominant turbulent component of the magnetic field, with the electric-vector polarization angle reduced by vector-averaging over the broad jet apparent opening angle. The high-resolution images of the jet (see Figure 9) confirm that the EVPA is parallel to the jet. Feature J1 usually has a high PD, indicating a moderate degree of ordering of the magnetic field, while J2 is too close to the core to evaluate its PD.

At optical wavelengths, we also observe emission from a larger volume in the jet than at X-ray energies, with an EVPA within the range of directions of the broad jet. Some of the optical emission also comes from the inner jet region. Because of this, we observe global optical flux enhancement in 2023 August, with respect to 2022 October (with a peak observed in the V filter simultaneous with the X-ray maximum), and optical polarimetric variability.

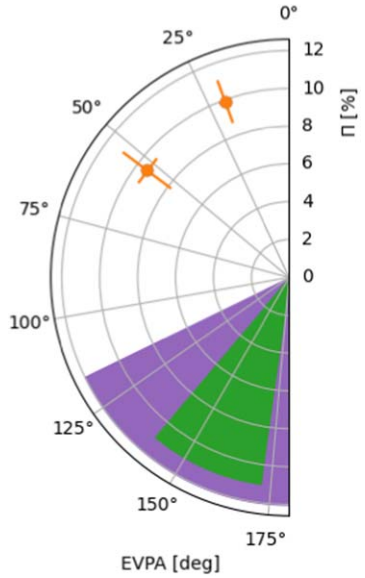

Figure 12. X-ray polarization results (orange symbols) and comparison with radio-jet direction: purple area represents the projected radio jet reported in Z. R. Weaver et al. (2022); green area represents the mean radio jet direction from the position angle of knot J1.

X-rays are emitted from a more compact region very close to the site of the highest-energy particle acceleration, allowing us to probe the local magnetic field associated with the acceleration process. The X-ray EVPAs are almost orthogonal to the overall jet direction as defined by the VLBA images; see Figure 12 and Z. R. Weaver et al. (2022). Three rough sketches of possible scenarios are presented in Figures 13, 14, and 15 (see also A. P. Marscher et al. 2024). In Figure 13, we assume that plasma is accelerated by local magnetic reconnection in a turbulent zone where oppositely directed magnetic fields stochastically meet. Most X-rays and a small fraction of the observed optical photons are emitted in the magnetic reconnection region, with a polarization angle that is essentially random and unrelated to the jet direction. Farther downstream of the accelerating region, the magnetic field includes a component transverse to the jet axis. This could be the result of a weak helical or toroidal field component (M. Lyutikov et al. 2005) or mild compression by shocks (P. A. Hughes et al. 1985). Optical photons are also emitted in this region. The relatively long cooling time of electrons responsible for the optical emission smooths the flaring profile in the optical light curve (see F. Tavecchio 2021, for further discussion).

In an alternative scenario, sketched in Figure 14, the jet is twisted by a few degrees, amplified by projection effects owing to the small angle of the axis to the line of sight. The X-ray emission is produced close to the jet origin, with the particle acceleration mechanism unspecified. The jet bends such that the EVPA in the X-ray emitting region happens to lie roughly perpendicular to the downstream jet direction where the 43 GHz core is observed.

The cartoon in Figure 15 represents a scenario that includes a helical magnetic field in the X-ray emission region that could explain the rotating EVPA signals inferred from our analysis above. This could be incorporated into the first scenario

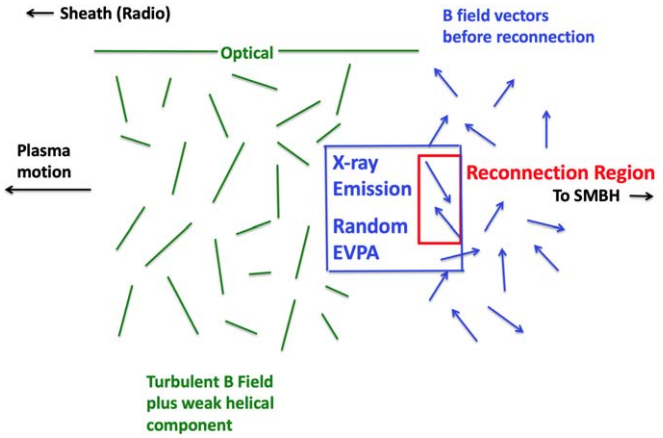

Figure 13. Sketch of possible model for a structured jet in 1ES 1959+650. The X-ray emission arises from a small volume in turbulent plasma where magnetic reconnection occurs, accelerating electrons to extremely high energies. The magnetic field is randomly oriented, with no relation to the jet direction. The optical and radio emission occur downstream, where a helical component of the magnetic field (or weak shocks) provides a net field direction transverse to the jet axis.

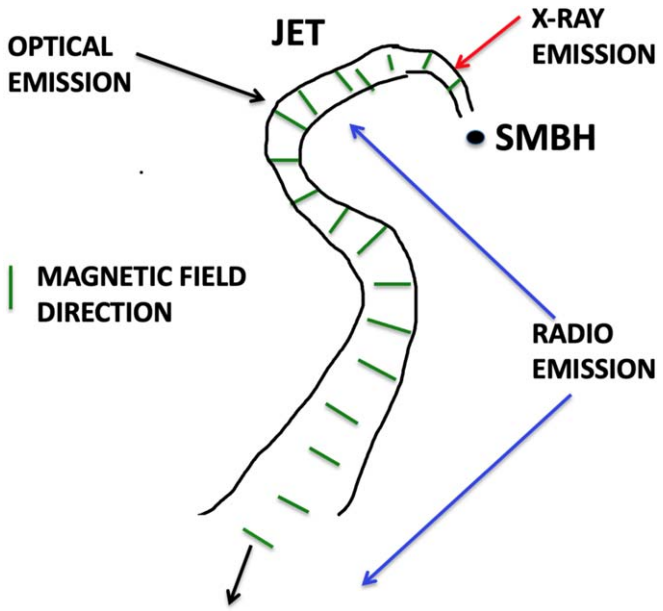

Figure 14. Sketch of a second possible model designed to explain observation of the jet in 1ES 1959+650. The jet is slightly twisted, with bending by less than a few degrees that is accentuated by projection effects. The magnetic field is locally transverse to the jet axis along the jet's length, owing to a weak helical field component or mild shocks. The X-ray emission arises from an upstream region with different EVPA (which is transverse to the field) than that of the lower-frequency emission radiated in the downstream regions.

(Figure 13) if there is a small helical field component in the magnetic reconnection region.

The variability we see in the X-ray EVPA is amplified by the effects of relativistic beaming, aberration, and Doppler shifts. We cannot state from our measurements alone whether the different magnetic field orientations (in X-ray with respect to optical and radio) are due to a spine-sheath structure of the jet (see, e.g., M. Georganopoulos & D. Kazanas 2003; G. Ghisellini et al. 2005; F. Tavecchio & G. Ghisellini 2008; and Figure 13), or if the magnetic field changes continuously from subparsec to parsec scales. In a previous short observation of 50 ks (in 2022 May), IXPE found a low-significance

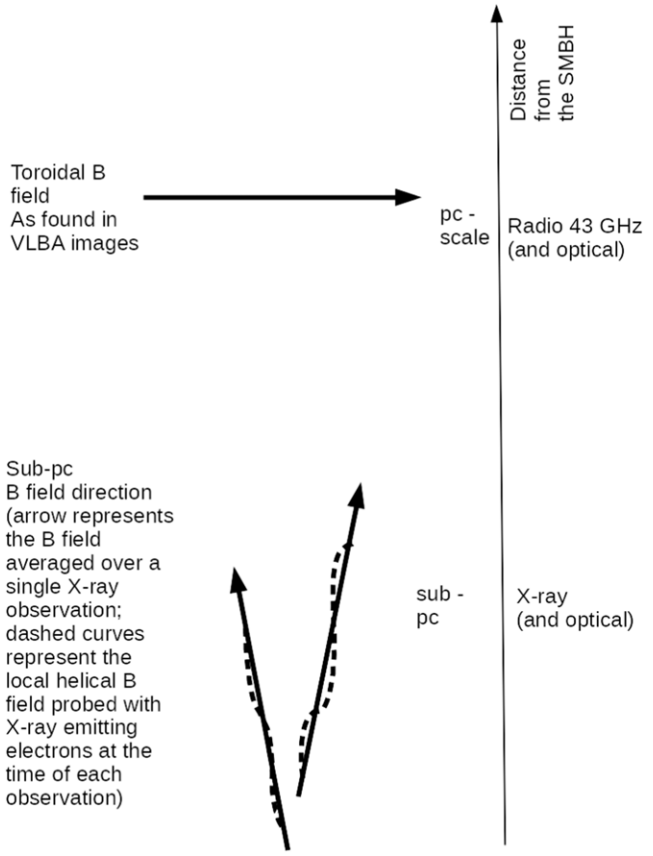

Figure 15. Sketch of a third scenario for explaining the X-ray polarization of 1ES 1959+650. X-rays probe subparsec scale distances from the SMBH, which contain a helical magnetic field with a small pitch angle (or, alternatively, a turbulent magnetic field with mean direction along the jet axis). Arrows indicate mean direction of the magnetic field during each of our two IXPE observations; X-ray EVPA is perpendicular to the mean magnetic field (projected on the sky). VLBA images exhibit a mainly toroidal magnetic field on parsec scales.

polarimetric signal, and an EVPA almost aligned with the VLBA jet (M. Errando et al. 2024). IXPE has measured EVPAs lying almost parallel to the jet position angle in other HBLs: PKS 2155−304 (P. M. Kouch et al. 2024) and Mrk 501 (C.-T. J. Chen et al. 2024, after averaging the EVPAs over all six IXPE observations). The change of X-ray EVPA with respect to the VLBA jet position angle is rather erratic in Mrk 421: in 2022 May, the EVPA was ∼51° from the VLBA jet axis (L. Di Gesu et al. 2022); in 2022 June, IXPE observed an EVPA rotation by more than 360° over ∼5 days (L. Di Gesu et al. 2023); in 2022 December, the X-ray EVPA was almost perpendicular to the VLBA jet axis (D. E. Kim et al. 2024), and a rotation of the EVPA with a two-component model was detected, so we can apply the scenario depicted in Figure 15; the IXPE observations in 2023 December revealed an EVPA direction changing from parallel to shifted by ∼46° with respect to the VLBA jet axis (W. P. Maksym et al. 2024, paper submitted).

7. Conclusions

Based on all of the IXPE observations of blazars, if HBL jets contain a helical magnetic field component on subparsec scales, the magnetic field appears not to have a stable configuration. This implies that we can observe different behavior of the

X-ray emission in different objects, and at different times in a single object. We can measure long rotations of the EVPA for the case of a magnetic field with symmetry axis along the line of sight (as in the case of Mrk 421 on 2022 June). If the helical magnetic field has a symmetry axis not perfectly aligned with the line of sight, we can still recognize EVPA rotations by applying the multicomponent model; in this case, we expect the average X-ray EVPA to be almost orthogonal to the VLBA jet axis. For large off-axis values of the magnetic field on subparsec scales, the EVPA could be parallel to the VLBA jet due to projection effects. We note that radio features in the VLBA images of 1ES 1959+650, PKS 2155−304, Mrk 421, and Mrk 501 generally move at subluminal speeds (B. G. Piner et al. 2008, 2010), implying that the radio jet is aligned within a few degrees of the line of sight. The turbulent magnetic field scenario on subparsec scales could be adopted too, even if it is disfavored as the explanation of the 2022 June IXPE observation of EVPA rotation in Mrk 421. The turbulence model predicts that EVPA rotation could be observed by chance, but the average EVPA should not necessarily be orthogonal to the VLBA jet direction.

The observed average X-ray EVPA of 1ES 1959+650 is transverse to the mean magnetic field direction. We have found variability of the EVPA from one observation to the next, possibly implying that the average magnetic field in the X-ray emitting region is time-variable.

Our results suggest the presence of either a helical magnetic field in the jet of 1ES 1959+650, and perhaps other HBLs, or stochastic processes controlling the direction of the magnetic field within the jet. Further data are needed to confirm this conclusion, define better the temporal distribution of the X-ray EVPA, define better the relationship between the X-ray and longer-wavelength emission regions, and determine whether stochastic or systematic processes dominate the X-ray EVPA variations.

Acknowledgments

The Imaging X-ray Polarimetry Explorer (IXPE) is a joint US and Italian mission. The US contribution is supported by the National Aeronautics and Space Administration (NASA) and led and managed by its Marshall Space Flight Center (MSFC), with industry partner Ball Aerospace (now, BAE Systems). The Italian contribution is supported by the Italian Space Agency (Agenzia Spaziale Italiana, ASI) through contract ASI-OHBI-2022-13-I.0, agreements ASI-INAF-2022-19-HH.0 and ASI-INFN-2017.13-H0, and its Space Science Data Center (SSDC) with agreements ASI-INAF-2022-14-HH.0 and ASI-INFN 2021-43-HH.0, and by the Istituto Nazionale di Astrofisica (INAF) and the Istituto Nazionale di Fisica Nucleare (INFN) in Italy. This research used data products provided by the IXPE Team (MSFC, SSDC, INAF, and INFN) and distributed with additional software tools by the High-Energy Astrophysics Science Archive Research Center (HEASARC), at NASA Goddard Space Flight Center (GSFC). Funding for this work was provided in part by contract 80MSFC17C0012 from the MSFC to MIT in support of the IXPE project. Support for this work was provided in part by NASA through the Smithsonian Astrophysical Observatory (SAO) contract SV3-73016 to MIT for support of the Chandra X-Ray Center (CXC), which is operated by SAO for and on behalf of NASA under contract NAS8-03060. The IAA-CSIC co-authors acknowledge financial support from the Spanish "Ministerio de Ciencia e Innovación" (MCIN/AEI/ 10.13039/501100011033) through the Center of Excellence Severo Ochoa award for the Instituto de Astrofiisica de Andalucìa-CSIC (CEX2021-001131-S), and through grants PID2019-107847RB-C44 and PID2022-139117NB-C44. Some of the data are based on observations collected at the Observatorio de Sierra Nevada, owned and operated by the Instituto de Astrofisica de Andalucìa (IAA-CSIC). Further data are based on observations collected at the Centro Astronómico Hispano-Alemán (CAHA), operated jointly by Junta de Andalucìa and Consejo Superior de Investigaciones Cientìficas (IAA-CSIC). The Submillimetre Array is a joint project between the SAO and the Academia Sinica Institute of Astronomy and Astrophysics and is funded by the Smithsonian Institution and the Academia Sinica. Maunakea, the location of the SMA, is a culturally important site for the indigenous Hawaiian people; we are privileged to study the cosmos from its summit.

The data in this study include observations made with the Nordic Optical Telescope, owned in collaboration by the University of Turku and Aarhus University, and operated jointly by Aarhus University, the University of Turku, and the University of Oslo, representing Denmark, Finland and Norway, the University of Iceland, and Stockholm University at the Observatorio del Roque de los Muchachos, La Palma, Spain, of the Instituto de Astrofisica de Canarias. The data presented here were obtained in part with ALFOSC, which is provided by the Instituto de Astrofisica de Andalucìa (IAA) under a joint agreement with the University of Copenhagen and NOT. E.L. was supported by Academy of Finland projects 317636 and 320045. We acknowledge funding to support our NOT observations from the Finnish Center for Astronomy with ESO (FINCA), University of Turku, Finland (Academy of Finland grant No. 306531). The research at Boston University was supported in part by National Science Foundation grant AST-2108622, NASA NuSTAR Guest Investigator subcontract through JPL (RSA no. 1691953), NASA Fermi Guest Investigator grants 80NSSC23K1507 and 80NSSC23K1508, and NASA Swift Guest Investigator grant 80NSSC22K0537. This study used observations conducted with the 1.8 m Perkins Telescope Observatory (PTO) in AZ (USA), which is owned and operated by Boston University. The above study is based in part on observations obtained with XMM-Newton, an ESA science mission with instruments and contributions directly funded by ESA Member States and NASA. This research has made use of data from the RoboPol program, a collaboration between Caltech, the University of Crete, IA-FORTH, IUCAA, the MPIfR, and the Nicolaus Copernicus University, which was conducted at Skinakas Observatory in Crete, Greece. I.L. was supported by the NASA Postdoctoral Program at the Marshall Space Flight Center, administered by Oak Ridge Associated Universities under contract with NASA. Partly based on observations with the 100 m telescope of the MPIfR (Max-Planck-Institut für Radioastronomie) at Effelsberg. Observations with the 100 m radio telescope at Effelsberg have received funding from the European Union's Horizon 2020 research and innovation program under grant agreement No. 101004719 (ORP). The Very Long Baseline Array is an instrument of the National Radio Astronomy Observatory. The National Radio Astronomy Observatory is a facility of the National Science Foundation operated by Associated Universities, Inc.

Facilities: Calar Alto, Effelsberg 100m radio telescope, IXPE, LX-200, NuSTAR, XMM Newton, NOT, Perkins, Skinakas observatory, SMA, Observatorio de Sierra Nevada (SNO), Swift (XRT and UVOT).

$$S(R_1, \Pi_1, \Psi_1, \Pi_2, \Psi_2, \omega) = -2\sum_i \ln[1 + \mu_i R_1 \Pi_1(\cos(2\Psi_1)\cos(2\psi_i) + \sin(2\Psi_1)\sin(2\psi_i)) + \mu_i(1 - R_1)\Pi_2(\cos(2\Psi_2^0)\cos(2(\psi_i - \omega t_i) + \sin(2\Psi_2^0)\sin(2(\psi_i - \omega t_i))] . \quad \text{(A3)}$$

Appendix A
Likelihood Estimator for the Two-component Model

The two-component model assumes that the polarized emission is obtained with two independent components: the first (steady) component with a fixed PD Π_1 and angle Ψ_1 (EVPA does not rotate), and a second (rotating) component characterized by a rotating EVPA with a constant rotation velocity ω_2, and fixed PD Π_2; the polarization angle of the rotating component at the beginning of the observation is denoted by $\Psi_2(t=0)$. In this simple model, parameters do not depend on energy. If the fluxes of the two components are F_1 and F_2, respectively, we define the relative fluxes of the two components as $R_1 = F_1/(F_1 + F_2)$ and $R_2 = F_2/(F_1 + F_2)$. We can parameterize the two components with Stokes parameters q_1, u_1, $q_2(t)$, $u_2(t)$ (with Stokes parameters for the second component that vary with time) or q_1, u_1, q_2^0, u_2^0 of the bicomponents, and with the angular velocity ω of the EVPA of the second component (where q_2^0 and u_2^0 are the Stokes parameters of the second component at $t=0$). We can generalize the event density proposed for the likelihood estimator in Equation (51) of H. L. Marshall (2021): The event density for the case of the two-component model should not be integrated over the time interval, because it changes with time owing to the polarization rotation. The event density in this case is

$$\begin{aligned}\lambda(E, \psi) = [&R_1(1 + \mu(E) q_1 \cos(2\psi) \\ &+ \mu(E) u_1 \sin(2\psi)) \\ &+ R_2(1 + \mu(E) q_2(t) \cos(2\psi) \\ &+ \mu(E) u_2(t) \sin(2\psi))] f_E A_E \, dt \, dE \, d\psi , \end{aligned} \quad \text{(A1)}$$

where we use the same notation adopted in H. L. Marshall (2021). The Stokes parameters (q_2, u_2) describe a rotation of the EVPA, and can be written $q_2(t) = \Pi_2 \cos(2(\Psi_2^0 + \omega t))$ and $u_2(t) = \Pi_2 \sin(2(\Psi_2^0 + \omega t))$. Using the Werner formulas twice, performing the same steps used in H. L. Marshall (2021) to obtain their Equations (51) through (54), and in the assumption of no energy dependence of polarization, we can obtain an expression for the likelihood estimator of the two-component model:

$$\begin{aligned}&-2\sum_i \ln[1 + \mu_i R_1 q_1 \cos(2\psi_i) + \mu_i R_1 u_1 \sin(2\psi_i) \\ &+\mu_i(1 - R_1) q_2^0 \cos(2(\psi_i - \omega t_i)) + \mu_i(1 - R_1) u_2^0 \sin(2(\psi_i - \omega t_i))].\end{aligned} \quad \text{(A2)}$$

Here, u_2^0, q_2^0 are the Stokes parameters for the rotating component evaluated at $t=0$. There are six physical parameters to describe the model (R_1, u_1, q_1, u_2^0, q_2^0, ω), but model fitting requires only five independent parameters, e.g.: $R_1 q_1$, $R_1 u_1$, $(1 - R_1) q_2^0$, $(1 - R_1) u_2^0$, and ω. With a few steps, we obtain an expression involving PD and EVPA of the bicomponents:

The last expression is the likelihood estimator used in this study.

We can rewrite Equation (A1) as

$$\begin{aligned}\lambda(E, \psi) = &[1 + \mu(E) q_T(t) \cos(2\psi) \\ &+ \mu(E) u_T(t) \sin(2\psi)] f_E \, A_E \, dt \, dE \, d\psi, \end{aligned} \quad \text{(A4)}$$

where $q_T(t) = R_1 q_1 + R_2 q_2(t)$, and $u_T(t) = R_1 u_1 + R_2 u_2(t)$. Equation (A4) shows the known Stokes summation rule for incoherent polarized components: at any given time, we can represent the two-component model in the (q, u) plane as a vector $(q_T(t), u_T(t))$ that is the weighted sum of (q_1, u_1) and $(q_2(t), u_2(t))$ with weights given by the relative fluxes R_1 and R_2 of the intervening components. For any given observation with a given exposure, the two-component model is represented in the (q, u) plane as a circle of the radius $R_2\Pi_2$, and with the offset $R_1\Pi_1$ from the origin of the coordinates. In general, the event density of a multicomponent model can be represented at any given time as the weighted sum of (q_i, u_i) with weights R_i corresponding to the relative flux of the i components:

$$\begin{pmatrix} q_T \\ u_T \end{pmatrix} = \sum_i R_i \begin{pmatrix} q_i \\ u_i \end{pmatrix}. \quad \text{(A5)}$$

Appendix B
Adding a Counterrotating Component to the Two-component Model (Three-component Model with Two Counterrotating Components)

Following the vectorial representation in Equation (A5), we can evaluate the effect of a counterrotating component in the (q, u) plane (with the counterrotating component having opposite rotation velocity with respect to the rotating component). In the simple case of a rotating and counterrotating component with the same phase at $t = 0$, the two components add together coherently because they have the same direction. After a quarter of a turn in the (q, u) plane, the two components have opposite directions, reducing the total PD. After a half turn in the (q, u) plane, the two components add coherently, but with an opposite direction with respect to the case at $t = 0$. After three-quarters of a turn, the situation is analogous to the case at a quarter of a turn, but with an opposite direction. In general, a model with three components (a constant polarization component and both rotating and counterrotating components) draws an ellipse in the (q, u) plane. The orientation of the axes of the ellipse depends on the relative phase of the rotating and counterrotating components. In the special case of oppositely rotating components with the same relative fluxes,

the ellipse reduces to a segment in the (q, u) plane; and the polarization vector oscillates within the segment.

The event density for this model (the three-component model with two counterrotating components) can be evaluated directly using the formalism of Equation (A5), within which the event density can be written as

$$\begin{pmatrix} q_T \\ u_T \end{pmatrix} = R_1 \begin{pmatrix} q_1 \\ u_1 \end{pmatrix} + R_2 \begin{pmatrix} q_2(t) \\ u_2(t) \end{pmatrix} + R_2^* \begin{pmatrix} q_2^*(t) \\ u_2^*(t) \end{pmatrix}. \quad \text{(B1)}$$

We can write the vectors (q_i, u_i) as the product of the PD of the i component and a unit vector $\hat{p}_i$ containing the information of the EVPA for the i component: $(q_i, u_i) = \Pi_i \hat{p}_i$. Expression (B1) can be rewritten as

$$\begin{aligned} \begin{pmatrix} q_T \\ u_T \end{pmatrix} &= R_1 \Pi_1 \hat{p}_1 + R_2 \Pi_2 \hat{p}_2 + R_2^* \Pi_2^* \hat{p}_2^* \\ &= R_1 \Pi_1 \hat{p}_1 + (R_2 \Pi_2 + R_2^* \Pi_2^*) \left[\frac{R_2 \Pi_2}{R_2 \Pi_2 + R_2^* \Pi_2^*} \hat{p}_2 + \left(1 - \frac{R_2 \Pi_2}{R_2 \Pi_2 + R_2^* \Pi_2^*} \right) \hat{p}_2^* \right]. \end{aligned} \quad \text{(B2)}$$

Appendix C
Details of the Analysis of X-Ray Data for the 2022 October Observation

In order to check the result of the unbinned log-likelihood analysis, we applied the binned analysis and the χ^2 statistics for both the constant model and the two-component model. The results are reported in Figure 5. While the binned analysis is less sensitive, we determined that the difference of χ^2 for the two nested models is close to the difference of the log-likelihood obtained with the unbinned analysis. Therefore, our results are validated.

We used Monte Carlo simulations to investigate the statistical distribution of ΔC, where C is the log-likelihood minimum, in the case of sets of data simulated with constant polarization: The two-component model has five parameters (including a frequency), while the constant polarization model has two parameters. With the candidate frequency of the rotating component fixed, ΔC for the two-component model relative to the constant polarization model has a χ^2 distribution with 2 dof. We also verified the ΔC distribution on real data: we analyzed all the IXPE observations of pointlike, nonblazar sources with a count rate <25 count s^{-1} performed within the first 2 yr of observations. Observations lasting more than 6 days were subdivided into slots at least 3 days long. We obtained a total of 142 slots. We tried frequencies from the base frequency ($0.5/T_{\rm exposure}$, where the factor 0.5 comes from the fact that the EVPA is confined within a 180° range) up to 10 turn day^{-1}. With the exclusion of Cyg X-3, we obtained that the ΔC distribution follows a χ^2 distribution when computed as a function of EVPA rotating frequency. For Cyg X-3, we were able to reconstruct the orbital frequency from the frequency scan. Therefore, we consider the statistics and the procedure to be validated with both simulations and real data. Moreover, with an ad-hoc scan, we were able to reconstruct the spinning frequency of the X-ray pulsar GX 301−2. We also applied the method to the IXPE observations of Mrk 421 on 2022 June. We obtained the same findings reported in L. Di Gesu et al. (2023). Finally, the method has been already used to find the EVPA rotation during the IXPE observation of Mrk 421 on 2022 December; and the result has been validated with χ^2 fit of X-ray polarimetric evolution of the source (D. E. Kim et al. 2024).

We estimate the number of trials from the frequency range we searched over (approximately 10 times the base frequency). While performing the frequency scan to minimize the log-likelihood estimator, we have to deal with random signals. Random signals in the frequency domain have a correlation width that corresponds to the base frequency, so the number of independent trials is the ratio of the frequency range divided by the frequency width of random signals. The scan on frequencies was performed for both positive and negative frequencies; hence, the frequency range should be multiplied by a factor of 2. We then have 20 independent trial frequencies. The chance probability can be obtained by using the binomial distribution for at least a signal with $\Delta C \geqslant 19.6$ and 20 trials. We then derive a probability of 1.1×10^{-3} that the two-component model provides a better fit to the data (with respect to the constant polarization model) by random chance.

Appendix D
Details of the Analysis of X-Ray Data for the 2023 August Observation

We studied with Monte Carlo simulations the case of applying the three-component model to event lists simulated with a constant EVPA and PD. The probability $P(\Delta C^*, N)$ to find by chance at least one signal with ΔC^* from a sample of N extractions depends on the probability p^* of extracting a value of ΔC^* in a single trial (which can be computed from the χ^2 distribution with 4 dof): $P(\Delta C^*, N) = \sum_{k=1}^{N} B(k, p^*)$, where $B(k, p)$ is the binomial distribution for k successes, and p is the probability of having a success in a single trial. With the chosen window length (Δt), random signals have a frequency width of $0.5/\Delta t$ in the frequency scan reported in Figure 7; we have 42 independent trials per window. For a single window, we have $P(\Delta C = 26.6, N = 42) = 1.0 \times 10^{-3}$, and $P(\Delta C = 20.5, N = 42) = 1.6\%$. If we consider that the search was performed on four staggered windows, the number of independent trials should be multiplied by a factor of $\leqslant 4$. Therefore, the chance probabilities are $\leqslant 4.0 \times 10^{-3}$ and 6.5% for the candidate frequencies at 5.2 ± 0.1 and 1.9 ± 0.1 turn day^{-1}, respectively.

We analyzed the folded polarimetric light curves reported in Figure 8 with a binned χ^2 method to validate the unbinned analysis for window 3. We tested the two nested hypotheses of the constant and three-component models. Results are shown in

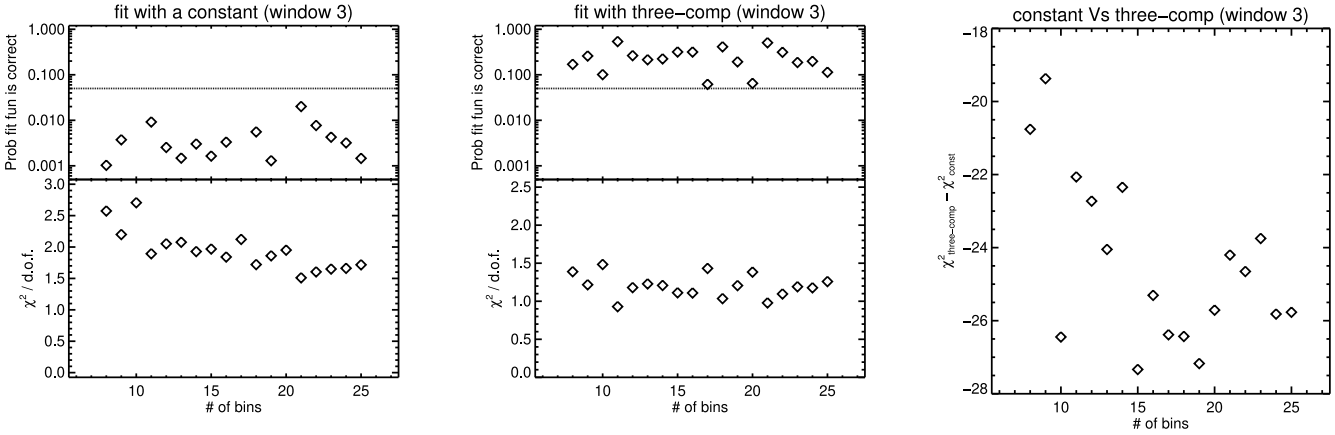

Figure 16. Results of binned analysis fitting of the 2023 August polarimetric light curve. Fit was performed on the q and u Stokes light curves. Left panel: reduced χ^2 for the constant polarization model as a function of the number of time bins, and associated probability that the fit function is true. Central panel: reduced χ^2 for the three-component polarization model as a function of the number of time bins, and associated probability that the fit function is true. Right panel: difference between the χ^2 for the three-component model and the χ^2 for the constant component as a function of the number of time bins.

Figure 16 as a function of the number of time bins. The $\Delta\chi^2$ between the constant and three-component models is $\Delta\chi^2 \sim 25$, confirming the unbinned likelihood result.

We tested with simulations whether the gaps in the observation could produce a spurious rotating polarization signal, but we were unable to reproduce any such signal. We also investigated whether the satellite dithering strategy could result in some characteristic frequency. In fact, noisy readout pixels, or charge buildup in the Gas Electron Multiplier (L. Baldini et al. 2021), combined with satellite dithering, could generate spurious, time variable polarization. Moreover, a spurious polarization measurement can be obtained for a source with a projected image close to the detector boundaries (A. Di Marco et al. 2023). We analyzed attitude data of the IXPE satellite, and studied the angular displacements of the source position (in detector D1 frame) with respect to the x- and y-axis of the D1 frame, along the radial direction, and rotations about the normal axis. We found several typical frequencies: the lower frequencies are at 14.9 day^{-1} (the satellite orbital frequency) and at 64.9 day^{-1}, with similar strength (we also found secondary harmonics and a beat frequency at 50 day^{-1}), incompatible with our results. In order to verify the effect on polarization results, we executed a further analysis of our window 3 data subset, extending the frequency scan over the first main frequency. We found only a weak signal, with $\Delta C = -13.7$ peaking at 14.84 day^{-1}, that could be tentatively correlated with the dithering strategy. This weak signal obtained for window 3 is not confirmed over the entire integration, for which we should expect a cumulative amplitude. Hence, we conclude that the combined effect of dithering and charge buildup has a negligible effect on the polarization rotation for a source photon count rate of $\sim$2 cts s^{-1}.

ORCID iDs

Luigi Pacciani https://orcid.org/0000-0001-6897-5996
Dawoon E. Kim https://orcid.org/0000-0001-5717-3736
Riccardo Middei https://orcid.org/0000-0001-9815-9092
Herman L. Marshall https://orcid.org/0000-0002-6492-1293
Alan P. Marscher https://orcid.org/0000-0001-7396-3332
Ioannis Liodakis https://orcid.org/0000-0001-9200-4006
Iván Agudo https://orcid.org/0000-0002-3777-6182
Svetlana G. Jorstad https://orcid.org/0000-0001-6158-1708
Juri Poutanen https://orcid.org/0000-0002-0983-0049
Manel Errando https://orcid.org/0000-0002-1853-863X
Laura Di Gesu https://orcid.org/0000-0002-5614-5028
Michela Negro https://orcid.org/0000-0002-6548-5622
Fabrizio Tavecchio https://orcid.org/0000-0003-0256-0995
Kinwah Wu https://orcid.org/0000-0002-7568-8765
Chien-Ting Chen https://orcid.org/0000-0002-4945-5079
Fabio Muleri https://orcid.org/0000-0003-3331-3794
Lucio Angelo Antonelli https://orcid.org/0000-0002-5037-9034
Immacolata Donnarumma https://orcid.org/0000-0002-4700-4549
Steven R. Ehlert https://orcid.org/0000-0003-4420-2838
Francesco Massaro https://orcid.org/0000-0002-1704-9850
Stephen L. O'Dell https://orcid.org/0000-0002-1868-8056
Matteo Perri https://orcid.org/0000-0003-3613-4409
Simonetta Puccetti https://orcid.org/0000-0002-2734-7835
Giacomo Bonnoli https://orcid.org/0000-0003-2464-9077
Pouya M. Kouch https://orcid.org/0000-0002-9328-2750
Emmanouil Angelakis https://orcid.org/0000-0001-7327-5441
Alexander Kraus https://orcid.org/0000-0002-4184-9372
Matteo Bachetti https://orcid.org/0000-0002-4576-9337
Luca Baldini https://orcid.org/0000-0002-9785-7726
Wayne H. Baumgartner https://orcid.org/0000-0002-5106-0463
Ronaldo Bellazzini https://orcid.org/0000-0002-2469-7063
Stefano Bianchi https://orcid.org/0000-0002-4622-4240
Stephen D. Bongiorno https://orcid.org/0000-0002-0901-2097
Raffaella Bonino https://orcid.org/0000-0002-4264-1215
Alessandro Brez https://orcid.org/0000-0002-9460-1821
Niccoló Bucciantini https://orcid.org/0000-0002-8848-1392
Fiamma Capitanio https://orcid.org/0000-0002-6384-3027
Simone Castellano https://orcid.org/0000-0003-1111-4292
Elisabetta Cavazzuti https://orcid.org/0000-0001-7150-9638
Stefano Ciprini https://orcid.org/0000-0002-0712-2479
Enrico Costa https://orcid.org/0000-0003-4925-8523
Alessandra De Rosa https://orcid.org/0000-0001-5668-6863
Ettore Del Monte https://orcid.org/0000-0002-3013-6334
Niccoló Di Lalla https://orcid.org/0000-0002-7574-1298

Alessandro Di Marco https://orcid.org/0000-0003-0331-3259
Victor Doroshenko https://orcid.org/0000-0001-8162-1105
Michal Dovčiak https://orcid.org/0000-0003-0079-1239
Teruaki Enoto https://orcid.org/0000-0003-1244-3100
Yuri Evangelista https://orcid.org/0000-0001-6096-6710
Sergio Fabiani https://orcid.org/0000-0003-1533-0283
Riccardo Ferrazzoli https://orcid.org/0000-0003-1074-8605
Javier A. Garcia https://orcid.org/0000-0003-3828-2448
Shuichi Gunji https://orcid.org/0000-0002-5881-2445
Jeremy Heyl https://orcid.org/0000-0001-9739-367X
Wataru Iwakiri https://orcid.org/0000-0002-0207-9010
Philip Kaaret https://orcid.org/0000-0002-3638-0637
Vladimir Karas https://orcid.org/0000-0002-5760-0459
Fabian Kislat https://orcid.org/0000-0001-7477-0380
Jeffery J. Kolodziejczak https://orcid.org/0000-0002-0110-6136
Henric Krawczynski https://orcid.org/0000-0002-1084-6507
Fabio La Monaca https://orcid.org/0000-0001-8916-4156
Luca Latronico https://orcid.org/0000-0002-0984-1856
Simone Maldera https://orcid.org/0000-0002-0698-4421
Alberto Manfreda https://orcid.org/0000-0002-0998-4953
Frédéric Marin https://orcid.org/0000-0003-4952-0835
Andrea Marinucci https://orcid.org/0000-0002-2055-4946
Giorgio Matt https://orcid.org/0000-0002-2152-0916
Tsunefumi Mizuno https://orcid.org/0000-0001-7263-0296
C.-Y. Ng https://orcid.org/0000-0002-5847-2612
Nicola Omodei https://orcid.org/0000-0002-5448-7577
Chiara Oppedisano https://orcid.org/0000-0001-6194-4601
Alessandro Papitto https://orcid.org/0000-0001-6289-7413
George G. Pavlov https://orcid.org/0000-0002-7481-5259
Abel Lawrence Peirson https://orcid.org/0000-0001-6292-1911
Melissa Pesce-Rollins https://orcid.org/0000-0003-1790-8018
Pierre-Olivier Petrucci https://orcid.org/0000-0001-6061-3480
Maura Pilia https://orcid.org/0000-0001-7397-8091
Andrea Possenti https://orcid.org/0000-0001-5902-3731
Brian D. Ramsey https://orcid.org/0000-0003-1548-1524
John Rankin https://orcid.org/0000-0002-9774-0560
Ajay Ratheesh https://orcid.org/0000-0003-0411-4243
Oliver J. Roberts https://orcid.org/0000-0002-7150-9061
Roger W. Romani https://orcid.org/0000-0001-6711-3286
Carmelo Sgró https://orcid.org/0000-0001-5676-6214
Patrick Slane https://orcid.org/0000-0002-6986-6756
Paolo Soffitta https://orcid.org/0000-0002-7781-4104
Gloria Spandre https://orcid.org/0000-0003-0802-3453
Douglas A. Swartz https://orcid.org/0000-0002-2954-4461
Toru Tamagawa https://orcid.org/0000-0002-8801-6263
Roberto Taverna https://orcid.org/0000-0002-1768-618X
Allyn F. Tennant https://orcid.org/0000-0002-9443-6774
Nicholas E. Thomas https://orcid.org/0000-0003-0411-4606
Francesco Tombesi https://orcid.org/0000-0002-6562-8654
Alessio Trois https://orcid.org/0000-0002-3180-6002
Sergey S. Tsygankov https://orcid.org/0000-0002-9679-0793
Roberto Turolla https://orcid.org/0000-0003-3977-8760
Jacco Vink https://orcid.org/0000-0002-4708-4219
Martin C. Weisskopf https://orcid.org/0000-0002-5270-4240
Fei Xie https://orcid.org/0000-0002-0105-5826
Silvia Zane https://orcid.org/0000-0001-5326-880X

References

Ackermann, M., Anantua, R., Asano, K., et al. 2016, ApJL, 824, L20
Aharonian, F., Akhperjanian, A., Beilicke, M., et al. 2003, A&A, 406, L9
Aharonian, F., Akhperjanian, A. G., Bazer-Bachi, A. R., et al. 2007, ApJL, 664, L71
Aliu, E., Archambault, S., Arlen, T., et al. 2014, ApJ, 797, 89
Baldini, L., Barbanera, M., Bellazzini, R., et al. 2021, APh, 133, 102628
Baldini, L., Bucciantini, N., Lalla, N. D., et al. 2022, SoftX, 19, 101194
Blandford, R. D., & Königl, A. 1979, ApJ, 232, 34
Blinov, D., Kiehlmann, S., Pavlidou, V., et al. 2021, MNRAS, 501, 3715
Burrows, D. N., Hill, J. E., Nousek, J. A., et al. 2005, SSRv, 120, 165
Chandra, S., Boettcher, M., Goswami, P., et al. 2021, ApJ, 918, 67
Chen, C.-T. J., Liodakis, I., Middei, R., et al. 2024, ApJ, 974, 50
Di Gesu, L., Donnarumma, I., Tavecchio, F., et al. 2022, ApJL, 938, L7
Di Gesu, L., Marshall, H. L., Ehlert, S. R., et al. 2023, NatAs, 7, 1245
Di Marco, A., Costa, E., Muleri, F., et al. 2022, AJ, 163, 170
Di Marco, A., Soffitta, P., Costa, E., et al. 2023, AJ, 165, 143
Ehlert, S. R., Liodakis, I., Middei, R., et al. 2023, ApJ, 959, 61
Errando, M., Liodakis, I., Marscher, A. P., et al. 2024, ApJ, 963, 5
Georganopoulos, M., & Kazanas, D. 2003, ApJL, 594, L27
Ghisellini, G., Tavecchio, F., & Chiaberge, M. 2005, A&A, 432, 401
Hovatta, T., Lindfors, E., Blinov, D., et al. 2016, A&A, 596, A78
Hughes, P. A., Aller, H. D., & Aller, M. F. 1985, ApJ, 298, 301
Jorstad, S. G., Marscher, A. P., Larionov, V. M., et al. 2010, ApJ, 715, 362
Jorstad, S. G., Marscher, A. P., Morozova, D. A., et al. 2017, ApJ, 846, 98
Kapanadze, B. 2023, ATel, 16162, 1
Kapanadze, B., Dorner, D., Vercellone, S., et al. 2018, ApJS, 238, 13
Kim, D. E., Di Gesu, L., Liodakis, I., et al. 2024, A&A, 681, A12
Kouch, P. M., Liodakis, I., Middei, R., et al. 2024, A&A, 689, A119
Kraus, A., Krichbaum, T. P., Wegner, R., et al. 2003, A&A, 401, 161
Krawczynski, H., Hughes, S. B., Horan, D., et al. 2004, ApJ, 601, 151
Larionov, V. M., Jorstad, S. G., Marscher, A. P., et al. 2008, A&A, 492, 389
Liodakis, I., Marscher, A. P., Agudo, I., et al. 2022, Natur, 611, 677
Lyutikov, M., Pariev, V. I., & Gabuzda, D. C. 2005, MNRAS, 360, 869
MAGIC Collaboration, Acciari, V. A., Ansoldi, S., et al. 2020a, A&A, 638, A14
MAGIC Collaboration, Acciari, V. A., Ansoldi, S., et al. 2020b, A&A, 640, A132
Maksym, W. P., Liodakis, I., Saade, M. L., et al. 2024, arXiv:2410.19983
Marrone, D. P., & Rao, R. 2008, Proc. SPIE, 7020, 70202B
Marscher, A. P. 2014, ApJ, 780, 87
Marscher, A. P., Di Gesu, L., Jorstad, S. G., et al. 2024, Galax, 12, 50
Marshall, H. L. 2021, ApJ, 907, 82
Middei, R., Liodakis, I., Perri, M., et al. 2023a, ApJL, 942, L10
Middei, R., Perri, M., Puccetti, S., et al. 2023b, ApJL, 953, L28
Myserlis, I., Angelakis, E., Kraus, A., et al. 2018, A&A, 609, A68
Nakariakov, V. M., Anfinogentov, S. A., Nisticò, G., & Lee, D. H. 2016, A&A, 591, L5
Nilsson, K., Lindfors, E., Takalo, L. O., et al. 2018, A&A, 620, A185
Nilsson, K., Pasanen, M., Takalo, L. O., et al. 2007, A&A, 475, 199
Panopoulou, G., Tassis, K., Blinov, D., et al. 2015, MNRAS, 452, 715
Patel, S. R., Shukla, A., Chitnis, V. R., et al. 2018, A&A, 611, A44
Pei, Y. C. 1992, ApJ, 395, 130
Peirson, A. L., Negro, M., Liodakis, I., et al. 2023, ApJL, 948, L25
Perlman, E. S., Stocke, J. T., Schachter, J. F., et al. 1996, ApJS, 104, 251
Piner, B. G., Pant, N., & Edwards, P. G. 2008, ApJ, 678, 64
Piner, B. G., Pant, N., & Edwards, P. G. 2010, ApJ, 723, 1150
Poole, T. S., Breeveld, A. A., Page, M. J., et al. 2008, MNRAS, 383, 627
Primiani, R. A., Young, K. H., Young, A., et al. 2016, JAI, 5, 1641006
Rector, T. A., Gabuzda, D. C., & Stocke, J. T. 2003, AJ, 125, 1060
Roming, P. W. A., Kennedy, T. E., Mason, K. O., et al. 2005, SSRv, 120, 95
Sault, R. J., Teuben, P. J., Wright, M. C. H., et al. 1995, in ASP Conf. Ser. 77, Astronomical Data Analysis Software and Systems IV, ed. R. A. Shaw, H. E. Payne, & J. J. E. Hayes (San Francisco, CA: ASP), 433
Sorcia, M., Benìtez, E., Hiriart, D., et al. 2013, ApJS, 206, 11
Tagliaferri, G., Foschini, L., Ghisellini, G., et al. 2008, ApJ, 679, 1029
Tavecchio, F. 2021, Galax, 9, 37
Tavecchio, F., & Ghisellini, G. 2008, MNRAS: Letters, 385, L98
Urry, C. M., & Padovani, P. 1995, PASP, 107, 803
Weaver, Z. R., Jorstad, S. G., Marscher, A. P., et al. 2022, ApJS, 260, 12
Weisskopf, M. C., Soffitta, P., Baldini, L., et al. 2022, JATIS, 8, 026002